3-15-2016

Phase field approach to dislocation evolution at large strains: Computational aspects

Mahdi Javanbakht
Isfahan University of Technology

Valery I. Levitas
Iowa State University, vlevitas@iastate.edu

Phase field approach to dislocation evolution at large strains: Computational aspects

Abstract
Computational aspects of the phase field simulations of dislocation nucleation and evolution are addressed. The complete system of equations for the coupled phase field approach to dislocation nucleation and evolution and nonlinear mechanics for large strains is formulated. Analytical solutions for a stationary and propagating single dislocation, dislocation velocity, core energy, and core width are found. Dislocation parameters for nickel are identified based on existing molecular dynamics simulations. In contrast to all previous efforts that are based on the spectral approach, finite element method (FEM) is utilized, which allowed us to treat large strain problems and non-periodic boundary conditions. The single dislocation order parameter profile and the stationary distance between two neighboring dislocations at a semicoherent sharp austenite–martensite interface are in perfect agreement with analytical expressions. The main focus is on proving that the new points of the developed theory can be confirmed in simulations, including possibility of obtaining the desired dislocation height for aligned and inclined dislocations, eliminating spurious stresses, resolving dislocation cores and interaction between cores of different dislocations. Mesh independence of the solutions is demonstrated and the effect of approximating finite element polynomials is analyzed, exhibiting possibility of significant numerical errors when special care is not taken of. Problems of nucleation and evolution of multiple dislocations along the single and multiple slip systems near martensitic lath, and along the sharp austenite –martensite interface, the activity of dislocations with two different orientations in a nanograined material under shear and pressure, and the interaction between two intersecting dislocation systems are studied. Surface-modified partial dislocation was revealed. These problems represent the first step in the future study of interaction of phase transformation and dislocations.

Keywords
Phase field simulation, Dislocations, Large strains, Nanoscale, Finite element method

Disciplines
Aerospace Engineering | Structures and Materials

Comments
This article is published as Javanbakht, Mahdi, and Valery I. Levitas. "Phase field approach to dislocation evolution at large strains: Computational aspects." International Journal of Solids and Structures 82 (2016): 95-110. doi: 10.1016/j.ijsolstr.2015.10.021. Posted with permission.

Phase field approach to dislocation evolution at large strains: Computational aspects

Mahdi Javanbakht

Isfahan University of Technology, Department of Mechanical Engineering, Isfahan, Iran

Department of Aerospace Engineering, Iowa State University, Ames, Iowa 50011, U.S.A.

Valery I. Levitas

Department of Aerospace Engineering, Iowa State University, Ames, Iowa 50011, U.S.A.

Department of Mechanical Engineering, Iowa State University, Ames, Iowa 50011, U.S.A.

Material Science and Engineering, Iowa State University, Ames, Iowa 50011, U.S.A.

Abstract

Computational aspects of the phase field simulations of dislocation nucleation and evolution are addressed. The complete system of equations for the coupled phase field approach to dislocation nucleation and evolution and nonlinear mechanics for large strains is formulated. Analytical solutions for a stationary and propagating single dislocation, dislocation velocity, core energy, and core width are found. Dislocation parameters for nickel are identified based on existing molecular dynamics simulations. In contrast to all previous efforts that are based on the spectral approach, finite element method (FEM) is utilized, which allowed us to treat large strain problems and non-periodic boundary conditions. The single dislocation order parameter profile and the stationary distance between two neighboring dislocations at a semicoherent sharp austenite - martensite interface are in perfect agreement with analytical expressions. The main focus is on proving that the new points of the developed theory can be confirmed in simulations, including possibility of obtaining the desired dislocation height for aligned and inclined dislocations, eliminating spurious stresses, resolving dislocation cores and interaction between cores of different dislocations. Mesh independence of the solutions is demonstrated and the effect of approximating finite element polynomials is analyzed, exhibiting possibility of significant numerical errors when special care is not taken of. Problems of nucleation and evolution of multiple dislocations along the single and multiple slip systems near martensitic lath, and along the sharp austenite - martensite interface, the activity of dislocations with two different orientations in a nanograined material under shear and pressure, and the interaction between two intersecting dislocation systems are studied. Surface-modified partial dislocation was revealed. These problems represent the first step in the future

Email address: vlevitas@iastate.edu (Valery I. Levitas)

study of interaction of phase transformation and dislocations.

Keywords: Phase field simulation; Dislocations; Large strains; Nanoscale; Finite element method

1. Introduction

Dislocational plasticity have been widely studied using continuum theories, see the recent papers [6, 12, 21, 28, 29, 33, 37, 80, 86]. At the nanoscale, phase field theories for dislocations are broadly used for modeling plasticity [2, 3, 8, 13, 22, 27, 30, 31, 32, 47, 48, 49, 53, 79, 81, 82, 83, 84, 85]. Quite sophisticated and physically interesting and important problems are solved, increasing our understanding of plasticity. It is surprising, however, that traditionally in computational mechanics studies on the accuracy and mesh-sensitivity of numerical solutions are almost absent. Thus, it is mentioned in [8] that in order to obtain a continuous profile of the order parameter for a dislocation within a core, the grid size should be 0.1 of the interplanar distance. However, such a fine grid has practically never been used in simulations. In [49] the accuracy of the stress distribution due to a single dislocation and ways to avoid significant oscillations were considered, with a grid size which was 10 times larger than the Burgers vector. Thus, there was no possibility to resolve the dislocation core and stresses were away from the dislocation core, i.e., long-range stresses. In the most practical, larger-scale simulations [79, 82, 84], the grid size is even 100 times of the interplanar distance.

Mesh dependence of the solutions was not studied because it was assumed in [8, 49, 79, 82, 84] that the dislocation height is equal to the mesh size, i.e., the dislocation height is mesh-dependent and non-objective by definition. As it was discussed in [70, 75], this assumption is made because the dislocation height was not defined by a theory and the system of equations is ill-posed. Traditionally, such formulations are inadmissible in computational mechanics. For similar problems on shear band localization in classical plasticity, a huge literature exists and the problem is regularized using a viscoplastic (e.g., [38]) or (in most cases) a gradient-type regularization (see, e.g., [1, 23]). This led, in particular, to a significant progress in gradient plasticity. Similar efforts are lacking in the phase field simulations of dislocations as well. As we will show below, dislocations are not localized within a single intergrid band, rather they produce bands with a height of 1 to 10 and more mesh sizes. This can be interpreted as 1 to 10 dislocations in the neighboring parallel planes, but this is unrealistic. Even if the dislocation was localized within one finite element, the interface Σ with the normal $\boldsymbol{n}$ between the dislocation band and the rest of the crystal has theoretically zero width. As we will demonstrate below, this leads to high oscillating internal shear stresses at the interface Σ which have two opposite effects. First, the huge artificial stresses can exceed the critical stress for dislocations and lead to an artificial nucleation of new

dislocations. Second, these artificial stresses generate an artificial elastic energy at the interface, which suppresses dislocation motion. Such stresses and a way to suppress them have not been studied yet. Also, there is no description in the literature on how to handle dislocations inclined with respect to the grid.

When using a regular grid, the localization of a dislocation band within one intergrid space leads to a small number of points to resolve the dislocation core profile along the slip direction, which results to wrong values for the width and the energy. In addition, a rough discretization leads to creating an artificial athermal threshold [49], which may arrest dislocations.

Another source of inaccuracy is related to the fact that when the Burgers vector is linearly dependent on the order parameters η (like in [2, 3, 8, 13, 22, 27, 30, 31, 32, 47, 48, 49, 53, 79, 81, 82, 83, 84, 85]), the thermodynamically equilibrium value of η, and consequently the equilibrium Burgers vector, depend on the stress tensor $\boldsymbol{\sigma}$. This was found in [67] analytically and then studied in [49] numerically. It was demonstrated in [49] that the stress-dependent Burgers vector changes the stress field of a dislocation and consequently its velocity. Nonlinear dependencies for the Burgers vector, which lead to constant, stress-independent equilibrium Burgers vector have been suggested in [49, 67, 75]. However, as it was shown in [75], the nonlinear dependence in [49] leads to an unrealistic equilibrium stress - order parameter curve, which requires infinite stresses for the lattice instability (theoretical strength). In general, the local equilibrium stress-strain curve and the theoretical shear strength were not analyzed for the previous models, until it was done in [67, 75].

All previous phase field simulations (e.g., in [8, 31, 32, 49, 79, 81, 82, 84]) were based on small strain (i.e., < 0.1) theory, which allowed one to use effective spectral methods for the problem solution combined with Khachaturyan-Shatalov microelasticity theory. This also implied periodic boundary conditions. At the same time, local shear strain for n dislocations is huge and is of the order of magnitude of n.

In the papers [70, 75], the phase field equations for dislocation nucleation and evolution at the nanoscale were derived from thermodynamics laws for large strains and were simplified for small strains as well. The Ginzburg-Landau equations are obtained as the linear kinetic relations between the rate of change of the order parameters and the conjugate thermodynamic driving forces. Several main shortcomings of the previous phase field studies have been resolved. In particular, large strain kinematics is introduced and it is done in a way consistent with phenomenological crystal plasticity. Also, expression for the Helmholtz free energy is advanced in the following directions:

(a) it reproduces the desired, mesh-independent height of dislocation bands for any slip system orientation and prevents dislocation widening;

(b) it excludes the localization of dislocation within a band of a smaller height than the prescribed one but does not produce artificial interface energy;

(c) it penalizes the interaction of different dislocations at the same point;

(d) it allows us to generate desired lattice instability conditions and a stress - order parameter curve, as well as to obtain stress-independent equilibrium Burgers vector and to avoid artificial dissipation during elastic deformation.

Non-periodic boundary conditions for dislocations are introduced, which include the change of the surface energy due to the exit of dislocations from the crystal.

All the above theoretical results make it possible to significantly advance the computational mechanics aspect and the strictness and the accuracy of the simulation of dislocation behavior. This is the main goal of the current paper. The main focus is on proving that the new points of the developed theory can be confirmed in simulations, including the possibility of obtaining the desired dislocation height for aligned and inclined dislocations, eliminating spurious stresses, resolving dislocation cores and the interaction between cores of different dislocations.

First, analytical solutions for a stationary and propagating single dislocation, dislocation velocity, core energy, and core width are found. Dislocation parameters for nickel are identified based on the results of molecular dynamics simulations in [14]. They also include the effect of the gradient term along the dislocation height. In contrast to all previous efforts that utilize the spectral approach, FEM is applied, which allowed us to treat large strain problems and non-periodic boundary conditions. In particular, free external surface is considered, for which the boundary condition looks different than for phase transformations. The single dislocation order parameter profile and the stationary distance between two neighboring dislocations at a semicoherent sharp austenite - martensite interface are in perfect agreement with analytical expressions. Note that the last problem has a shear strain equal to 3, i.e., the large strain formulation is tested to some extend as well. For a system of multiple parallel dislocations, it is shown that one can indeed obtain an objective solution with the prescribed dislocation height and eliminate artificial stresses at the boundary between the dislocation band and the rest of the crystal or between different dislocation bands. For non-optimal meshes and types of finite elements, solutions may differ significantly from the objective (correct) ones, with different numbers of dislocations, averaged stresses, and huge spurious oscillating stresses between the dislocation band and the rest of the crystal or between different dislocation bands. For models without the prescribed dislocation height, the solution is strongly mesh-dependent, with different numbers of dislocation bands of different widths, even for a small change of mesh. It was also demonstrated that inclined dislocations can be described without any problem, independent of the mesh, and the interaction of dislocations cores may essentially

change the local and global behaviors.

The solved problems include the nucleation and the evolution of multiple dislocations along the single and multiple slip systems, near a martensitic lath and along a sharp austenite - martensite interface, the activity of dislocations with two different orientations in a nanograined material under shear and pressure, and the interaction between two intersecting dislocation systems are studied. All these problems represent the first step in the future study of the interaction between phase transformations and plasticity. Some preliminary simulation results are presented in our short letter [70].

We designate contractions of tensors $\boldsymbol{A}$ and $\boldsymbol{B}$ over one and two indices as $\boldsymbol{A}\cdot\boldsymbol{B}$ and $\boldsymbol{A}:\boldsymbol{B}$; summation is assumed over the repeated indices. In some cases, when it is desirable to show the limits of summations, the sign $\sum$ will be used. Superscripts T and -1 designate transposed and inverse tensors, and superscript s is used for symmetric part of a tensor. Symbols with subscript 0 referrs to a parameter in the undeformed states; subscripts e and p designate elastic and plastic parts of deformation gradient or strain.

2. Complete system of equations and problem formulation

The complete system of equations derived in [70, 75] in the reference and deformed configurations, as well as for small strain approximation is summarized in Box 1.

Box 1. Complete system of equations

1. Kinematics

I. Large strains

1.1. Multiplicative decomposition of the deformation gradient $\boldsymbol{F}$ into elastic $\boldsymbol{F}_e$ and plastic $\boldsymbol{F}_p$ contributions

$$\boldsymbol{F} := \partial \boldsymbol{r}/\partial \boldsymbol{r}_0 = \nabla_0 \boldsymbol{r} = \boldsymbol{F}_e \cdot \boldsymbol{F}_p, \tag{1}$$

where $\boldsymbol{r} = \boldsymbol{r}(\boldsymbol{r}_0, t)$ is the location of a material point $\boldsymbol{r}_0$ of a body at time t. The points $\boldsymbol{r}_0$ and $\boldsymbol{r}$ form the reference (undeformed) Ω_0 and actual (deformed) Ω configurations, respectively.

1.2. Jacobian determinants

$$J := \frac{\rho_0}{\rho} = det\boldsymbol{F}; \quad J_e := \frac{\rho_p}{\rho} = det\boldsymbol{F}_e; \quad J_p := det\boldsymbol{F}_p = 1; \qquad J = J_e, \tag{2}$$

where ρ_0, ρ_p and ρ are the mass densities in the reference (undeformed), intermediate stress-free, and deformed configurations, respectively.

1.3. Rate of plastic deformation gradient

$$\dot{\boldsymbol{F}}_p = \sum_{\alpha=1}^{p} \left[\gamma_\alpha \boldsymbol{m}_0^\alpha \otimes \boldsymbol{n}_0^\alpha \dot{\Phi}(\bar{\eta}_\alpha)\right] \cdot \boldsymbol{F}_p;$$
$$\Phi = Int(\eta_\alpha) + \bar{\eta}_\alpha^2(3 - 2\bar{\eta}_\alpha); \qquad \bar{\eta}_\alpha := \eta_\alpha - Int\,(\eta_\alpha) \in [0, 1], \tag{3}$$

where $\boldsymbol{b}_0^\alpha$ is the the Burgers vector of a dislocation in the α^{th} slip system, $\boldsymbol{m}_0^\alpha$ is the unit vector in the direction of $\boldsymbol{b}_0^\alpha$, $\boldsymbol{n}_0^\alpha$ is the unit normal to the slip plane (all three are defined in the reference configuration), $\gamma_\alpha = |\boldsymbol{b}_0^\alpha|/H^\alpha$ is the plastic shear strain per single dislocation in a dislocation band of the height H^α, η_α is the order parameter for a dislocation in the α^{th} slip system, and $Int(\eta_\alpha)$ and $\bar{\eta}_\alpha$ are the integer and fractional parts of η_α.

II. Small strains

$$\boldsymbol{\varepsilon} = (\boldsymbol{\nabla u})_{\mathrm{s}} = \boldsymbol{\varepsilon}_e + \boldsymbol{\varepsilon}_p; \qquad \boldsymbol{\omega} = \boldsymbol{\omega}_e + \boldsymbol{\omega}_p; \quad \boldsymbol{\varepsilon}_p + \boldsymbol{\omega}_p = \sum_{\alpha=1}^{p} \frac{1}{H^\alpha} \boldsymbol{b}^\alpha \otimes \boldsymbol{n}^\alpha \Phi(\eta_\alpha), \tag{4}$$

where $\boldsymbol{u}$ is the displacement, $\boldsymbol{\varepsilon}$ and $\boldsymbol{\omega}$ are the small strain and rotations, respectively.

2. Helmholtz free energy ψ per unit mass

$$\psi = \psi^e(\boldsymbol{E}_e) + \psi^c + \psi^{int} + \psi^\nabla; \tag{5}$$

$$\rho_0 \psi^e(\boldsymbol{E}_e) = \frac{1}{2} \boldsymbol{E}_e \boldsymbol{:C:} \boldsymbol{E}_e; \tag{6}$$

$$\rho_0 \psi^{int} = \sum_{\alpha}^{p} \sum_{k=1}^{p} A_{\alpha k} \bar{\eta}_\alpha^2 (1 - \bar{\eta}_\alpha)^2 \bar{\eta}_k^2 (1 - \bar{\eta}_k)^2; \quad A_{\alpha\alpha} = 0; \tag{7}$$

$$\rho_0 \psi^\nabla = \frac{\beta}{2} \sum_{\alpha=1}^{p} \left\{ |\boldsymbol{\nabla}_0 \bar{\eta}_\alpha|^2 + [M(1 - \bar{\eta}_\alpha)^2 - 1](\boldsymbol{\nabla}_0 \bar{\eta}_\alpha \cdot \boldsymbol{n}_0^\alpha)^2 \right\}; \tag{8}$$

$$\rho_0 \psi^c = \sum_{\alpha=1}^{p} A_\alpha \bar{\eta}_\alpha^2 (1 - \bar{\eta}_\alpha)^2; \tag{9}$$

$$A_\alpha(y^\alpha) = \begin{cases} qA_\alpha^0 & \bar{y}^\alpha > H^\alpha; \\ A_\alpha^0 & \bar{y}^\alpha \le H^\alpha, \end{cases} \tag{10}$$
$$\bar{y}^\alpha = y^\alpha - Int(\frac{y^\alpha}{H^\alpha + w_\alpha})(H^\alpha + w_\alpha);$$

where ψ^e, ψ^c, ψ^∇, and ψ^{int} are the elastic, crystalline, and gradient energies as well as the energy of interaction of dislocation cores belonging to different slip systems, respectively, all per unit mass; $\boldsymbol{E}_e = 0.5(\boldsymbol{F}_e^T \cdot \boldsymbol{F}_e - \boldsymbol{I})$ is the elastic Lagrangian strain; $\boldsymbol{C}$ is the fourth-rank tensor of elastic moduli, A_α, $A_{\alpha k}$, and β are the crystalline energy, interaction energy, and gradient energy coefficients, respectively. Eq.(10) introduces the height H^α of the dislocation bands through the coefficient A_α, which is chosen to be a periodic step-wise function of the coordinate y^α along the normal to the slip plane $\boldsymbol{n}_0^\alpha$ and is equal to its normal value A_α^0 within each dislocation band of the height H^α and qA_α^0 ($q \gg 1$) in a thin boundary layer between dislocations of the width $w_\alpha = pH^\alpha$ ($p \ll 1$) (Fig. 1). Large values of A_α prevent the widening of the dislocation outside the designated dislocation band. Parameter M in the gradient energy is a small number penalizing gradient of the order parameter along $\boldsymbol{n}_0^\alpha$ and preventing localization of the dislocation within a band with a height smaller than the prescribed one, H^α.

3. First Piola-Kirchhoff $\boldsymbol{P}$ and Cauchy $\boldsymbol{\sigma}$ stress tensors

I. Large strains

$$\boldsymbol{P} = \rho_0 \boldsymbol{F}_e \cdot \frac{\partial \psi}{\partial \boldsymbol{E}_e} \cdot \boldsymbol{F}_p^{T-1}; \qquad \boldsymbol{\sigma} = \frac{\rho_0}{J} \boldsymbol{F}_e \cdot \frac{\partial \psi}{\partial \boldsymbol{E}_e} \cdot \boldsymbol{F}_e^T.$$

II. Small strains

$$\boldsymbol{\sigma} = \rho_0 \frac{\partial \psi}{\partial \boldsymbol{\varepsilon}_e}. \tag{11}$$

4. Ginzburg–Landau equations

4.1. Compact form in the reference configuration at large strains

$$\frac{1}{L}\frac{\partial \eta_\alpha}{\partial t} = X_\alpha = \frac{1}{\rho_0}\tau_\alpha \gamma_\alpha \frac{d\Phi}{d\eta_\alpha} - \frac{\partial \psi}{\partial \eta_\alpha} + \frac{1}{\rho_0}\boldsymbol{\nabla}_0 \cdot (\rho_0 \frac{\partial \psi}{\partial \boldsymbol{\nabla}_0 \eta_\alpha});$$

$$\tau_\alpha = J \boldsymbol{n}_0^\alpha \cdot \boldsymbol{F}_e^{-1} \cdot \boldsymbol{\sigma} \cdot \boldsymbol{F}_e \cdot \boldsymbol{m}_0^\alpha = \boldsymbol{n}_0^\alpha \cdot \boldsymbol{F}_p \cdot \boldsymbol{P}^T \cdot \boldsymbol{F}_e \cdot \boldsymbol{m}_0^\alpha, \tag{12}$$

where L is the kinetic coefficient, X_α is the thermodynamic driving force work-conjugate to $\dot{\eta}_\alpha$, and τ_α is the resolved shear stress.

4.2. Detailed form in the reference configuration at large strains

$$\frac{1}{L}\frac{\partial \eta_\alpha}{\partial t} = \frac{1}{\rho_0}\tau_\alpha\gamma_\alpha\frac{d\Phi}{d\eta_\alpha} - \frac{2}{\rho_0}A_\alpha\bar{\eta}_\alpha(1-\bar{\eta}_\alpha)(1-2\bar{\eta}_\alpha) \tag{13}$$
$$-\frac{2}{\rho_0}\bar{\eta}_\alpha(1-\bar{\eta}_\alpha)(1-2\bar{\eta}_\alpha)\sum_{k=1}^{p}A_{\alpha k}\bar{\eta}_k^2(1-\bar{\eta}_k)^2$$
$$+\beta\left\{\nabla_0^2\bar{\eta}_\alpha - 2M(1-\bar{\eta}_\alpha)(\boldsymbol{\nabla}_0\bar{\eta}_\alpha\cdot\boldsymbol{n}_0^\alpha)^2 + [M(1-\bar{\eta}_\alpha)^2-1](\boldsymbol{n}_0^\alpha\cdot\boldsymbol{\nabla}_0)(\boldsymbol{\nabla}_0\bar{\eta}_\alpha\cdot\boldsymbol{n}_0^\alpha)\right\}.$$

4.3. Compact form in the actual configuration at large strains

$$\frac{1}{L}\frac{D\eta_\alpha(\boldsymbol{r},t)}{Dt} = \frac{1}{L}\left(\frac{\partial\eta_\alpha(\boldsymbol{r},t)}{\partial t} + \boldsymbol{v}\cdot\boldsymbol{\nabla}\eta_\alpha\right) = \frac{1}{\rho_0}\tau_\alpha\gamma_\alpha\frac{d\Phi}{d\eta_\alpha} - \frac{\partial\psi}{\partial\eta_\alpha} + \frac{1}{\rho}\boldsymbol{\nabla}\cdot(\rho\frac{\partial\psi}{\partial\boldsymbol{\nabla}\eta_\alpha}), \tag{14}$$

where $\boldsymbol{v}$ is the particle velocity.

4.4. Detailed form in the actual configuration at large strains

$$\frac{1}{L}\frac{\partial \eta_\alpha}{\partial t} = \frac{1}{\rho_0}\tau_\alpha\gamma_\alpha\frac{d\Phi}{d\eta_\alpha} - \frac{2}{\rho_0}A_\alpha\bar{\eta}_\alpha(1-\bar{\eta}_\alpha)(1-2\bar{\eta}_\alpha) \tag{15}$$
$$-\frac{2}{\rho_0}\bar{\eta}_\alpha(1-\bar{\eta}_\alpha)(1-2\bar{\eta}_\alpha)\sum_{k=1}^{p}A_{\alpha k}\bar{\eta}_k^2(1-\bar{\eta}_k)^2$$
$$+\beta\left\{(\boldsymbol{F}\cdot\boldsymbol{F}^T)\boldsymbol{:}\boldsymbol{\nabla}\boldsymbol{\nabla}\bar{\eta}_\alpha - 2M(1-\bar{\eta}_\alpha)(\boldsymbol{\nabla}\bar{\eta}_\alpha\cdot\boldsymbol{n}^\alpha)^2 + [M(1-\bar{\eta}_\alpha)^2-1]\boldsymbol{n}^\alpha\cdot\boldsymbol{\nabla}\boldsymbol{\nabla}\bar{\eta}_\alpha\cdot\boldsymbol{F}\cdot\boldsymbol{F}^T{}_e\cdot\boldsymbol{n}^\alpha\right\}.$$

4.5. Small strains

$$\frac{1}{L}\frac{\partial \eta_\alpha}{\partial t} = \frac{1}{\rho_0}\tau_\alpha\gamma_\alpha\frac{d\Phi}{d\eta_\alpha} - \frac{2}{\rho_0}A_\alpha\bar{\eta}_\alpha(1-\bar{\eta}_\alpha)(1-2\bar{\eta}_\alpha)$$
$$-\frac{2}{\rho_0}\bar{\eta}_\alpha(1-\bar{\eta}_\alpha)(1-2\bar{\eta}_\alpha)\sum_{k=1}^{p}A_{\alpha k}\bar{\eta}_k^2(1-\bar{\eta}_k)^2$$
$$+\beta\left\{\nabla^2\bar{\eta}_\alpha - 2M(1-\bar{\eta}_\alpha)(\boldsymbol{\nabla}\bar{\eta}_\alpha\cdot\boldsymbol{n}^\alpha)^2 + [M(1-\bar{\eta}_\alpha)^2-1]\boldsymbol{n}^\alpha\cdot\boldsymbol{\nabla}\boldsymbol{\nabla}\bar{\eta}_\alpha\cdot\boldsymbol{n}^\alpha\right\}. \tag{16}$$

5. Momentum balance equation

I. Large strains

$$\boldsymbol{\nabla}_0\boldsymbol{\cdot}\boldsymbol{P} + \rho_0\boldsymbol{f} = \rho_0\dot{\boldsymbol{v}}; \qquad \boldsymbol{\nabla}\boldsymbol{\cdot}\boldsymbol{\sigma} + \rho\boldsymbol{f} = \rho\frac{D\boldsymbol{v}}{Dt}, \tag{17}$$

where $\boldsymbol{f}$ is the body force.

II. Small strains

$$\boldsymbol{\nabla}\boldsymbol{\cdot}\boldsymbol{\sigma} + \rho\boldsymbol{f} = \rho\dot{\boldsymbol{v}}. \tag{18}$$

6. Boundary conditions for the order parameters

I. Large strains

$$\boldsymbol{b}_0{}^{\alpha} \cdot \boldsymbol{\nabla}_0 \eta_\alpha = 0; \qquad \boldsymbol{\nabla} \eta_\alpha \cdot \boldsymbol{F} \cdot \boldsymbol{F}_e^{-1} \cdot \boldsymbol{b}^{\alpha} = 0. \tag{19}$$

II. Small strains

$$\boldsymbol{b}^{\alpha} \cdot \boldsymbol{\nabla} \eta_\alpha = 0. \tag{20}$$

As it is shown in [75], the above system of equations satisfies some important conditions for homo-

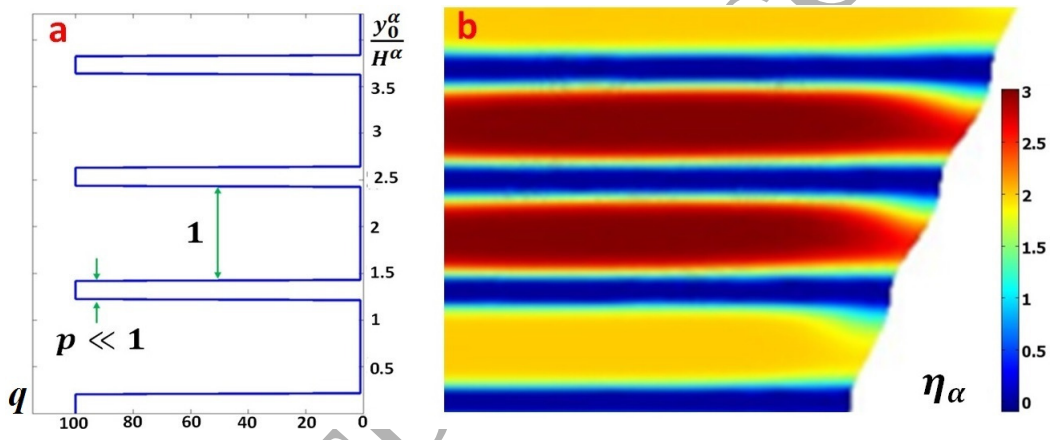

Fig. 1: (a) Distribution of the multiplier q in the expression for the barrier $A_\alpha = qA_\alpha^0$ in the crystalline energy, along the normal to each slip plane. It is equal to 1 within the slip band and 100 in a thin boundary layer between dislocations of the width $w_\alpha/H^\alpha = p$ $(p \ll 1)$. (b) Corresponding distribution of the order parameter η_α for dislocations.

geneous states after dislocations passed through the volume under study. First, $X_\alpha(\eta_\alpha = n_\alpha) = 0$ for any stresses, i.e., integer number of dislocations at any point corresponds to the thermodynamic equilibrium with respect to change of the order parameter. This allowed us to obtain constant (stress-independent) Burgers vector for complete dislocations. The second condition is

$$\frac{\partial^2 \psi(\boldsymbol{E}_e, \eta_i = n_i)}{\partial \eta_\alpha \partial \eta_k}\Big|_{\boldsymbol{E}_e} = 0; \quad \forall\, k \neq \alpha. \tag{21}$$

It significantly simplifies thermodynamic instability conditions for the homogeneous equilibrium states and allows one to obtain the desired lattice instability conditions and a stress-order parameter curve.

3. Parameter identification

In this Section, we will utilize results of molecular dynamics (MD) simulations from [14] for nickel to determine all material parameters. For this purpose, we will use an analytical solution for a single dislocation.

For a single dislocation band with the height of H^α in the y direction (coinciding with $\boldsymbol{n}_0^\alpha$) propagating along the x direction (coinciding with $\boldsymbol{b}_0^\alpha$), for η_α independent of y within a band of the height H^α the Ginzburg-Landau equation (13) is simplified as

$$\frac{1}{L/\rho_0}\frac{\partial \eta_\alpha}{\partial t} = 6\tau_\alpha\gamma_\alpha\bar{\eta}_\alpha(1-\bar{\eta}_\alpha) - 2A_\alpha\bar{\eta}_\alpha(1-\bar{\eta}_\alpha)(1-2\bar{\eta}_\alpha) + \rho_0\beta\frac{\partial^2\bar{\eta}_\alpha}{\partial x^2}. \tag{22}$$

Eq.(22) is formally similar to the Ginzburg-Landau equation for a plane austenite-martensite interface (Eq.(6)) for $a = 3$ in [61]. Therefore, we can use the analytical solutions Eqs.(10) and (13) in [61] for the propagating interface with the parameters $s_1 = A_\alpha - 3\tau_\alpha\gamma_\alpha$ and $s_2 = \tau_\alpha\gamma_\alpha$ in order to describe propagation of the dislocation band

$$\eta_\alpha(x,t) = \frac{1}{1+exp(-\frac{\sqrt{4A_\alpha-13\tau_\alpha\gamma_\alpha}}{\sqrt{2\rho_0\beta}}(x-vt))}. \tag{23}$$

with the dislocation velocity

$$v = \frac{L\tau_\alpha\gamma_\alpha\sqrt{\beta}}{\sqrt{2\rho_0(4A_\alpha-13\tau_\alpha\gamma_\alpha)}}. \tag{24}$$

For small stresses considered in [14], Eq.(24) simplifies to

$$v = \frac{L\tau_\alpha\gamma_\alpha\sqrt{\beta}}{2\sqrt{2\rho_0 A_\alpha}}. \tag{25}$$

For zero stresses τ_α, static solution

$$\eta_\alpha(x) = \frac{1}{1+exp(-\sqrt{2A_\alpha/(\rho_0\beta)}(x-x_0))}. \tag{26}$$

possesses the dislocation core energy per unit dislocation length and the dislocation core width

$$E = \frac{H^\alpha\sqrt{A_\alpha\rho_0\beta}}{3\sqrt{2}}; \quad \delta = \left[\frac{d\Phi(\bar{\eta}_\alpha(x))}{dx}\right]^{-1}_{max} = 2.667\sqrt{\frac{\rho_0\beta}{2A_\alpha}} \tag{27}$$

similar to the interface energy and width in [61]. However, energy in Eq.(27) contains a factor H^α, which is not present in the interface energy. This is because dislocation has a height H^α and

dislocation energy is per unit length, while interface energy is per unit area. The $\bar{\eta}_\alpha$ profile in our simulations is in a perfect agreement with the analytical expression (Fig. 2). To determine the

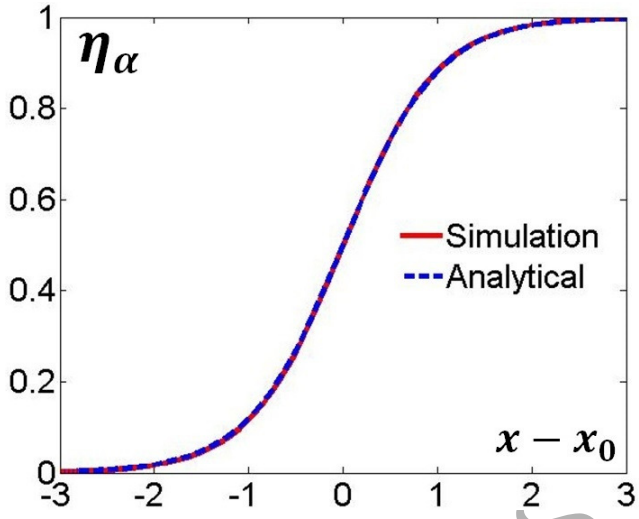

Fig. 2: Stationary dislocation profile of our simulation and comparison with analytical expression (length is normalized by $|\boldsymbol{b}_0^\alpha| = 0.35$).

material parameters A_α, β, and L, we use the results of molecular dynamics (MD) simulation from [14] for nickel. Namely, the dislocation core energy per unit dislocation length is $E = 0.28eV/\,\mathring{A} = 0.448 \times 10^{-9} J/m$; mobility $\frac{dv}{d\tau_\alpha} = 13.5\frac{nm}{psGPa}$; and the crystalline energy barrier per unit area of the gamma surface $\breve{A}_\alpha = 10.448 J/m^2$, which is related to our barrier A_α per unit volume as $\breve{A}_\alpha = A_\alpha H^\alpha$. Also, for nickel $\rho_0 = 8900 kg/m^3$. Using the interatomic distance $d = 0.35nm$ [14] and $H^\alpha = 2d = 0.7nm$, we obtain from this equation $A_\alpha = 14.93GPa$. Then Eq. (27) for energy results in $\beta = 5.55 \times 10^{-14} m^4/s^2$, after which Eq.(25) leads to $L = 5.2 \times 10^9 s/m^2$. Other parameters are: $|\boldsymbol{b}_0^\alpha| = 0.25nm$, $\gamma_\alpha = |\boldsymbol{b}_0^\alpha|/H^\alpha = 0.36$, $\tau_c^\alpha = A_\alpha/(3\gamma_\alpha) = 13.82GPa$, and $\delta = 1.37|\boldsymbol{b}_0^\alpha| = 0.343nm$.

Note that following the same procedure for a plane austenite-martensite interface in [61], a similar analytical solution for propagating dislocation is obtained in [14] but with some misprints. Also, since dislocation height was not resolved in [14], it was not present in the dislocation energy (27). That is why our parameters A_α and $\rho_0\beta$ are equal to the corresponding parameters in [14] divided by dislocation height H^α. Also, in Eq.(22), we use $\rho_0\beta$ as the pre-factor for Laplacian while in [14] it is chosen as 2β.

One more important point is that similar to a diffuse phase interface width, there are different ways to define the dislocation core width, which result in different pre-factors in Eq.(27). The definition in Eq.(27) was based on the maximum slope of function $\Phi(\bar{\eta}_\alpha)$, which characterizes variation of the Burgers vector. Alternatively, similar to a diffuse phase interface width in [69], a dislocation core can be defined as a length along which $\Phi(\bar{\eta}_\alpha)$ varies between 0.01 to 0.99; then the

dislocation core width can be expressed as $\delta_2 = 5.54\sqrt{\frac{\rho_0\beta}{2A_\alpha}}$. This leads to a broader dislocation core $\delta_2 = 2.83|\boldsymbol{b}_0^\alpha| = 0.71nm$.

Note that the dislocation core width in [14] was defined based on the slope of the $\bar{\eta}_\alpha$ profile (Eq.(20) from [14]) rather than slope of $\Phi(\bar{\eta}_\alpha)$ profile. While $\Phi(\bar{\eta}_\alpha)$ characterizes variation of the Burgers vector, $\bar{\eta}_\alpha$ alone does not have specific meaning and such a definition is less preferable.

The above results were obtained for the case when η_α is independent of y and the regularizing term with M does not participate in the solution. However, in numerical simulations η_α depends on y and additional energy scaled with M has to be taken into account. Thus, in order to obtain the same dislocation core energy as in [14], we need to find the corresponding parameters β and M from our simulations. The larger M, the smaller stress oscillations at the surface Σ. However, the contribution of the gradient of the order parameters along the normal $\boldsymbol{n}$ to the slip plane, $\nabla^n\eta$, to the total gradient energy increases, which is physically undesirable, because it is just a regularizing term. Thus, we use several values of M and choose the smallest one, which does not lead to significant oscillations. We presented in Fig. 3 the dislocation core energy for two different values of M, 1/100 and 1/20, and the variable β in some range. A comparison with the energy from the MD results gives $\beta = 2.25 \times 10^{-14} m^4/s^2$ for $M = 1/100$ and $\beta = 1.6 \times 10^{-14} m^4/s^2$ for $M = 1/20$. Our simulations demonstrated that for $M = 1/20$ the solution for η_α along the normal has the desired form (see Fig. 13) and small oscillations, while for $M = 1/100$ the regularization is not sufficient. That is why we use $M = 1/20$ in all simulations below.

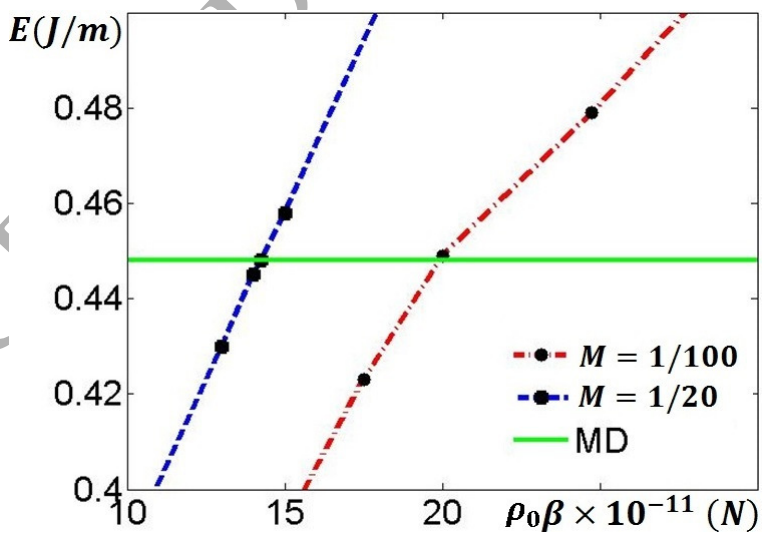

Fig. 3: The dislocation core energy for different values of $\rho_0\beta$ and two different values of M in comparison with that from MD simulations [14].

4. Results and discussion

Our simulations have been performed for a different material than Ni considered in Section 2, namely NiAl, with the same parameters as in [70]. This was done due to our interest in studying the interaction of plasticity and martensitic phase transformations [71, 72, 73, 74] and all of our results here are the first step for this study. None of the problems below was treated with the phase field approach previously. While Ni does not have phase transformations in solid state, NiAl undergoes a cubic to tetragonal phase transformation. Thus, the following parameters for all slip systems and homogeneous material have been used in all problems, unless stated differently: $|\boldsymbol{b}_0^\alpha| = 0.35nm$, $d = 0.35nm$, $H^\alpha = 2d = 0.7nm$, $\gamma_\alpha = 0.5$, $\rho_0 = 5850kg/m^3$, $\beta = 1.5\times10^{-14}m^4/s^2$, $A_\alpha = A = 1.43\times10^9 N/m$, $A_{\alpha k} = 0.143\times10^9 N/m$, $L = 8.9\times10^7 s/m^2$ and $M = 1/20$. These values, in particular, correspond to $E = 0.75\times10^{-10}J/m$, $\delta = 5.54\sqrt{\frac{\beta}{2A_\alpha}} = 0.97nm = 2.77|\boldsymbol{b}_0^\alpha|$, and $\tau_c^\alpha = 0.96GPa$. Parameters in the periodic crystalline energy are $k = 100$ and $w_\alpha = 0.1H^\alpha$. The simplest isotropic linear elasticity is used with shear modulus $\mu = 71.5GPa$ and bulk modulus $K = 112.6GPa$. Boundary conditions Eq.(19) for the order parameters neglect change in surface energy when dislocations exit a sample. To generalize the results for a different material we normalize size, stress, and time parameters by $|\boldsymbol{b}_0^\alpha| = 0.35nm$, $\tau_c^\alpha = 0.96GPa$, and $\bar{t} = \rho_0/(A_\alpha L) = 0.07ps$, respectively. 28000 elements are used, where elements have the maximum size of 0.2 at the A-M interface, and the maximum size of 1 in the rest of the sample. FEM and code COMSOL Multiphysics with an embedded remeshing procedure was used. COMSOL applies remeshing automatically anytime during solution to eliminate large mesh distortion and/or mesh inversion and to avoid divergence. One can choose the time range during which remeshing is allowed and can control the range of mesh sizes. COMSOL does not necessarily change the whole mesh pattern, instead it automatically produces remeshing in local regions, mainly near stress concentrators, places where elements are drastically distorted, and when different types of meshes in different regions are utilized.

Different moduli of COMSOL have been utilized for the implementation of the above system of equations; the most general finite strain case requires an application of PDE (partial differential equations) modulus. The backward differentiation formula are used to solve the time dependent problem. Plane strain problems for straight edge dislocations are considered. Seven elements per dislocation height and 5 elements per width of a core are used. Quadrilateral type of elements with the second degree polynomial for the shape function is utilized unless otherwise stated. Compared to linear elements, quadrilateral elements reduce the total number of degrees of freedom and the computation time, as well as improve convergence in our problems. At least 5 elements are required

to reproduce the dislocation core profile. In some problems, the fifth degree polynomial for the shape function reduces significantly stress oscillations between the dislocation band and the rest of a crystal.

Several model problems will be solved in this section to illustrate the application of the developed approach. Main focus will be on demonstrating large strain effects and mesh-independence of the solution, reproducing an analytical expression for spacing between dislocations along the phase interface, the treatment of inclined dislocations and their interaction, and dislocation activity in a nanograin bicrystal.

4.1. Sharp austenite - martensite interface and incoherency dislocations

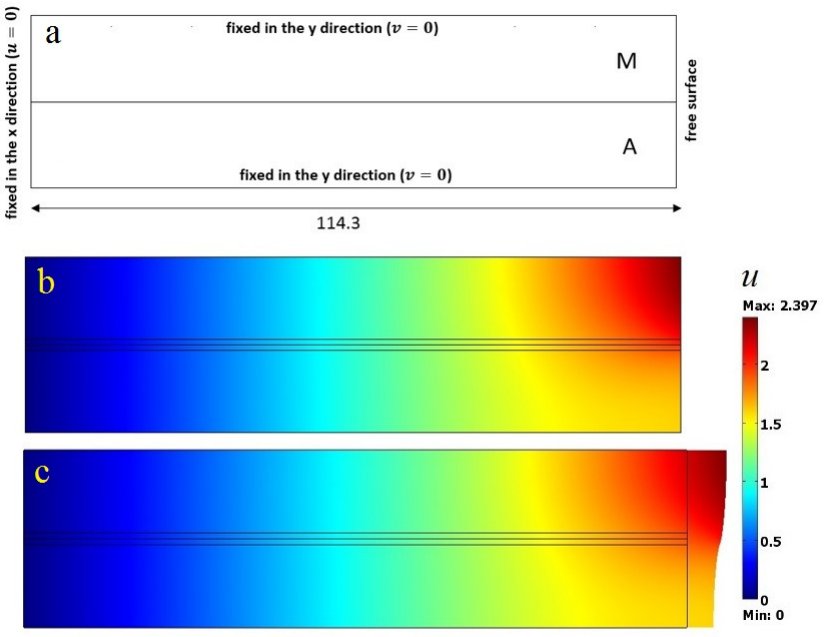

Fig. 4: Problem on dislocation evolution along the austenite-martensite interface. (a) Schematic and mechanical boundary conditions. (b) and (c) horizontal displacement field before appearance of the first dislocation in the initial undeformed and current deformed configurations, respectively.

For a coherent interface atomic positions in contacting lattices are continuous across the interface. The lattice continuity can be interrupted by misfit dislocations, which Burgers vector can be within interface or inclined to the interface. Incoherency dislocations determine the energy and mobility of interface, and consequently play an important role in determining thermodynamic, kinetics, nanostructure, and material properties, and have been of main interest in [11, 17, 18, 19, 26, 34, 35, 40, 41, 42, 45, 46, 52, 62, 77]. Here, we consider nucleation, evolution, and stationary incoherency dislocations inside a sharp austenite - martensite interface with Burgers

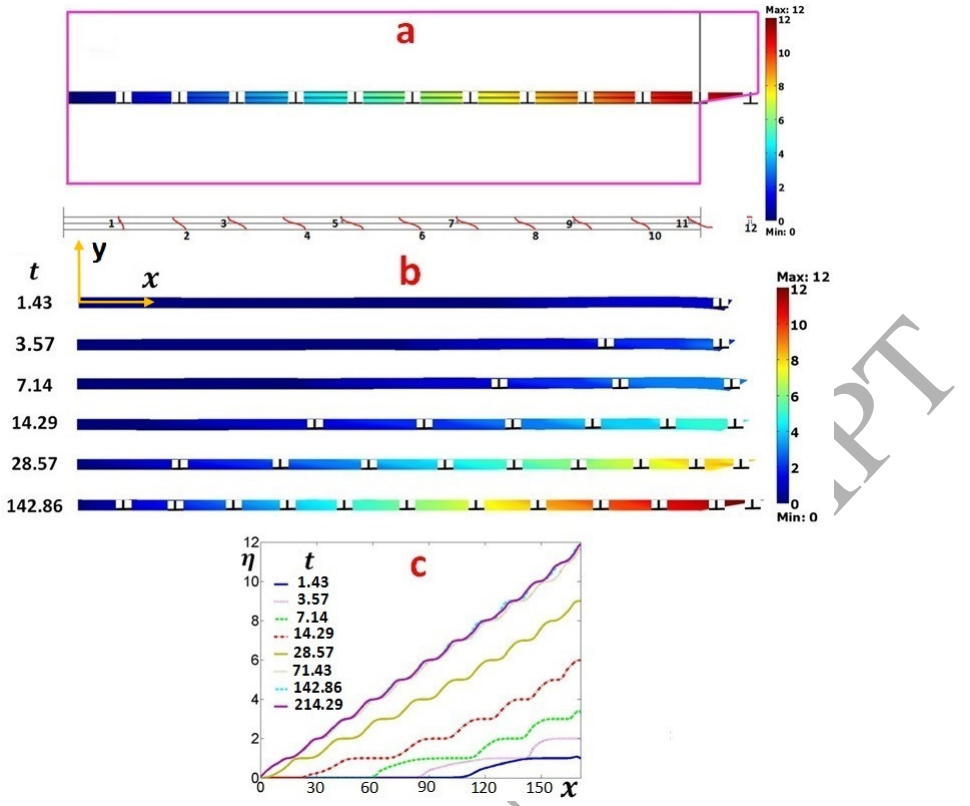

Fig. 5: (a) Stationary distribution of dislocations that nucleated at free surface and propagated along the sharp austenite - martensite interface with a misfit strain of 0.1 in the x direction. (b) The evolution of dislocations along the interface and (c) the corresponding dislocation profiles of η at the middle line of the dislocation band.

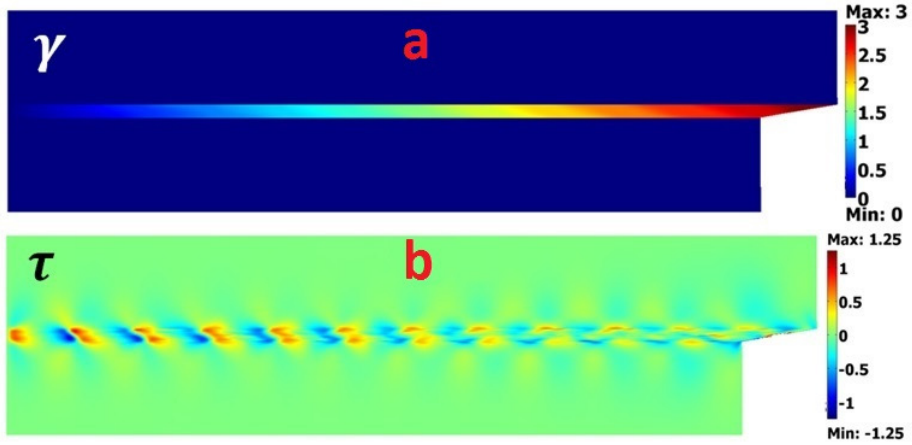

Fig. 6: (a) Stationary shear strain γ and (b) shear stress τ distributions for the stationary distribution of dislocations in Fig. 5a.

vectors belonging to the interface. A rectangle of the size of 30.6×114.3 was considered with the sharp austenite - martensite interface in the middle of it and in the middle of a dislocation band (Figs. 4 and 5). A misfit (transformation) strain of $\Delta = 0.1$ in the x direction is applied in the upper martensitic half of the sample as the eigen strain. The upper and lower sides are fixed in the y direction and the left side is fixed in the x direction; all other external stresses are zero. Also,

the plastic shear $\gamma_\alpha = 0.25$. The initial condition was $\eta = 0.01$ inside the dislocation band. Horizontal displacement field before appearance of the first dislocation in the initial undeformed and current deformed configurations, respectively, is presented in Fig. 4, (b) and (c). Displacements are continuous across an interface (i.e., it interface is coherent), which causes large elastic stresses due to the misfit strain. Next, twelve dislocations are generated from the free surface at the right side, and propagate along the interface and inside the dislocation band one after another (Fig. 5a). A dislocation sign shows the slip plane and normal to the slip plane (or the extra half plane of atoms) of a dislocation, as usual. Thus, a coherent interface transforms into a semicoherent one. The evolution of dislocations along the interface and the corresponding dislocation profiles of η at the middle line of the dislocation band are presented in Figs. 5b and c, respectively. In the stationary state, distance between any of two neighboring dislocations is 10, in perfect correspondence with the normalized analytical expression $1/\Delta$ [10]. Twelve dislocations produce a step at the free surface with shear strain of $n\gamma_\alpha = 3$, which means that large strain formulations are to some extend tested in this problem (Fig. 6a). The shear stress is concentrated inside the dislocation band as well and decays away from each band along the normal to the slip plane (Fig. 6b). They do not have any artificial oscillations. This problem represents the first step for studying thermodynamics, kinetics, and mechanisms of the propagation of semicoherent interfaces.

4.2. Objectivity and mesh-dependence

A square sample with the size of 28.6×28.6 was considered with the lower side fixed in both directions and the upper side fixed in the y direction. A horizontal displacement $u = 0.2t$ is applied at the upper side from $t = 0$ to 40. Initially, a dislocation nucleus of $\eta = 1$ with the size of 2×2 was considered at the middle of the right side of the sample and $\eta = 0.01$ everywhere else. For Figs. 7 and 8a, a dislocation system is considered only at the middle of the sample, the rest of a sample deforms elastically. The slip direction is along the x axis, and the plastic shear $\gamma_\alpha = 0.5$. The evolution of dislocations is presented in Fig. 7. Due to the applied shear, first dislocation propagates along the slip plane, and then 6 more dislocations are generated from the center of the dislocation band, one by another propagate along the x direction and leave the sample at the free surfaces, which create steps at both ends of the sample. Dislocations do not move outside of the prescribed dislocation system, and propagation is acceptably quasi-homogeneous. Corresponding stationary solution within a sample is shown in Fig. 8a. It is practically mesh-independent, which was checked by solutions for different meshes (Fig. 9).

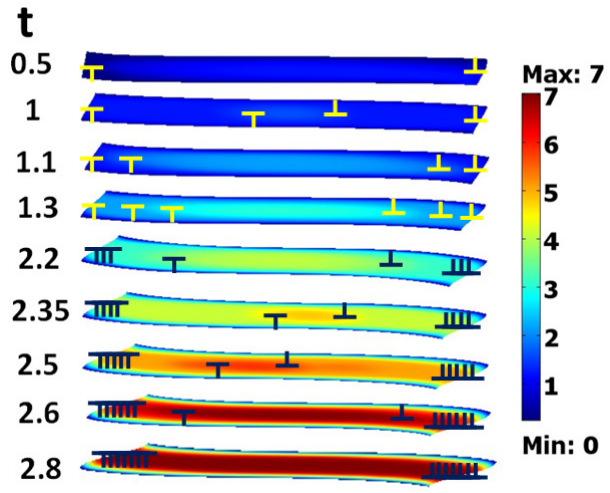

Fig. 7: The evolution of dislocations inside the dislocation band along the slip plane at the middle of a square sample under the prescribed shear displacement. The dislocation band is shown only.

If we do not consider the periodic step-wise function of the coordinate along the normal to the slip plane for the coefficient A_α and use the same coefficient A_α everywhere, as well as neglect the new gradient term normal to the slip plane ($M = 0$), similar to previous phase field studies for dislocations, solution is mesh-dependent. Figs. 8b-d show three different mesh patterns and their corresponding mesh-dependent solutions. Also, the order parameter η profiles along the normal to the slip plane at the right side of the sample are presented for the mesh-independent and the three mesh-dependent solutions in Fig. 10. As can be seen, for any of the mesh-dependent solutions, dislocation widening occurs. This is because of first, the lack of the intrinsic length along the normal to the slip plane and theoretically zero dislocation height, which leads to high oscillating internal shear stress at the boundary between any two neighboring elements normal to the slip plane which causing artificial nucleation of new dislocations, and second, the lack of a barrier normal to the slip plane to penalize the dislocation widening. For Fig. 8d, dislocations are generated separately in parallel slip planes which widen normal to their slip planes, and for larger prescribed shear coalesce with each other, finally filling the entire sample.

4.3. Suppressing effect of oscillating stresses at boundaries of the dislocation bands Σ *on dislocation evolution*

A rectangle with the size of 10×24.3 was considered with the upper and lower sides fixed in the y direction and the left bottom corner fixed in both directions (Fig. 11). This problem models dislocation activity near the martensitic lath [20, 24, 50, 51, 64], which is located at the left side of the sample and possesses transformation shear strain 0.3 (Fig. 12). Initially, there are no dislocations ($\eta = 0$), except in a small region with $\eta = 0.01$ along the austenite - martensite interface inclined under 63^0 with respect to the x direction. Elastic stresses cause nucleation and

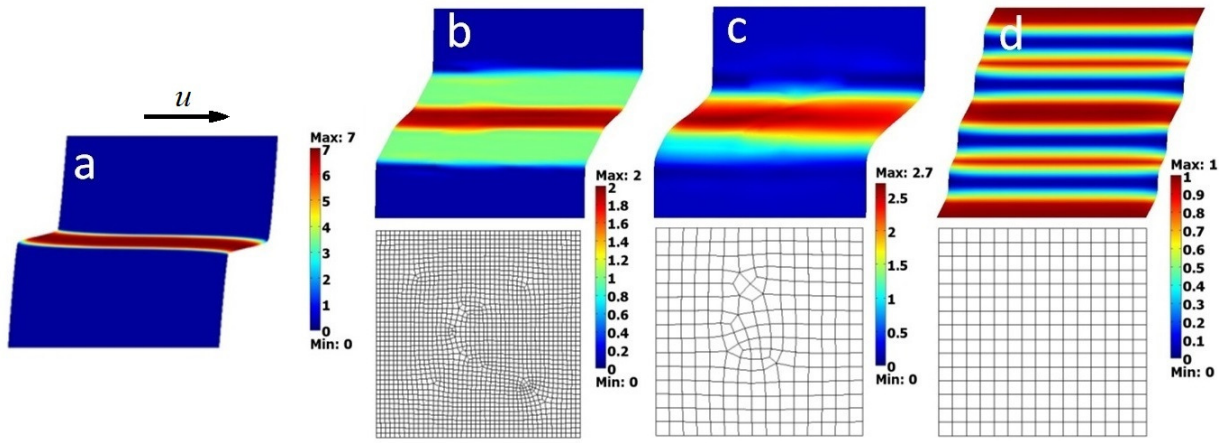

Fig. 8: (a) Mesh-independent solution of dislocations in a square sample under prescribed shear and (b)-(d) three different mesh patterns and corresponding mesh-dependent solutions when the periodic step-wise function of the coordinate along the normal to the slip plane for the coefficient A_α is not utilized and the gradient term normal to the slip plane is neglected, $M = 0$.

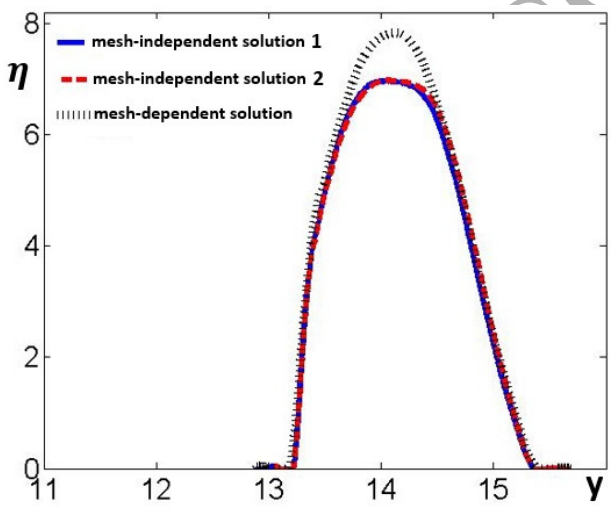

Fig. 9: Distribution of the order parameter for the problem in Fig. 8 (a) for 6 and 7 elements per dislocation height (mesh-independent solutions 1 and 2) and for 4 elements per dislocation height (mesh-dependent solution).

propagation of parallel dislocations, one after another, with several dislocations in each system in the stationary state. Relaxation of elastic stresses leads to the straightening of the initially curved interface. Closeness of different dislocations near the austenite-martensite interface means overlapping of their cores and stress fields, which is not easy to properly model with discrete dislocation dynamics. Dislocations do not move outside the prescribed bands, have clear horizontal boundaries (despite the unstructured FEM mesh), and propagate acceptably quasi-homogeneously. To elucidate the effect of oscillating stresses at boundaries of the dislocation bands Σ on dislocation propagation, the problem is solved for two different FEM approximations: one with the 2^{nd} degree interpolation polynomial in the FEM in space coordinates for both η and displacements (lower degree approximation (Fig. 12a)), and another with the 2^{nd} degree interpolation polynomial for

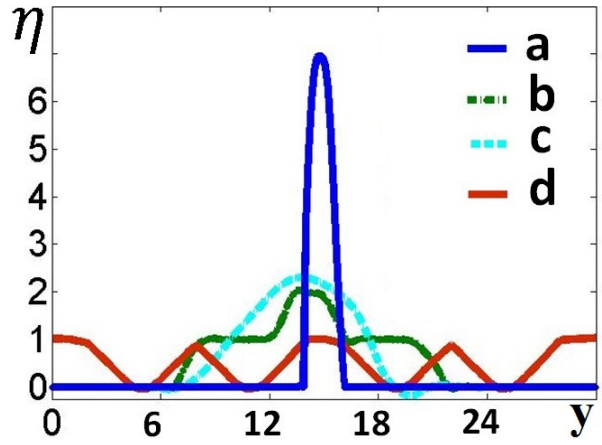

Fig. 10: Dislocation profiles along the normal to the slip plane at the right side of the sample for the mesh-independent solution (a) and three mesh-dependent solutions (b)-(d) in Fig. 8.

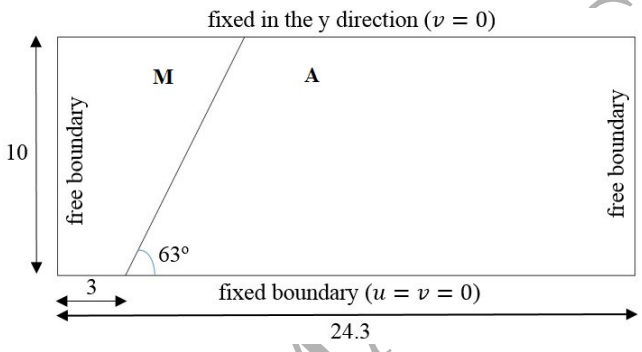

Fig. 11: Geometry and mechanical boundary conditions for the problem on dislocation activity near the martensitic lath.

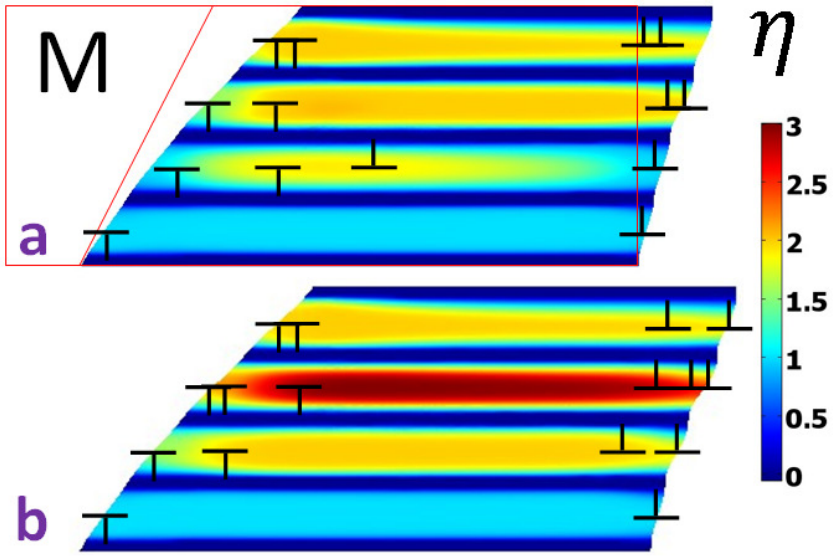

Fig. 12: Stationary solutions for a parallel dislocation systems under prescribed transformation shear strain of 0.3 in the martensitic part of a sample with the 2^{nd} degree interpolation polynomial in the FEM in space coordinates for both η and displacements (a), and with the 2^{nd} degree interpolation polynomial for η and 5^{th} degree polynomial for displacements (b).

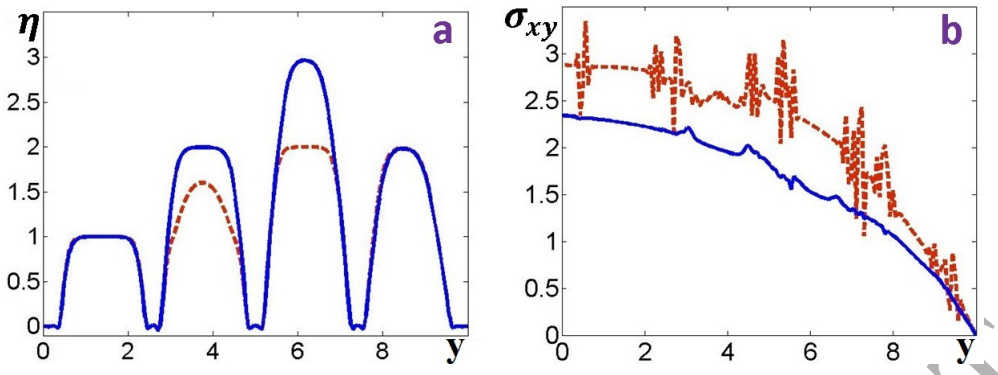

Fig. 13: (a) Distribution of the order parameter and (b) shear stress σ_{xy} at $t = 20$ for the 2^{nd} degree polynomial in space coordinates for η and the 5^{th} degree polynomial for displacements (blue solid line, mesh-independent solution), and for the 2^{nd} degree polynomial for both η and displacements (red dashed line).

η and 5^{th} degree polynomial for displacements (higher degree approximation (Fig. 12b)). One of the main natural requirements to the dislocation solution is that after the passing of dislocations through any chosen region, boundaries of the dislocation bands Σ do not generate internal stresses. For the lower degree polynomial, significant unphysical internal shear stresses (oscillations) at the boundaries Σ are present (Fig. 13b, red dashed line) even after the appearance of the first dislocation. These oscillations produce artificial interface energy, which suppresses propagation of dislocations; that is why solutions for different FEM approximations are different. At the same time, for the higher degree polynomial, internal stresses and oscillations are negligible (Fig. 13b, blue solid line) even after the appearance of multiple dislocations. The stationary solutions of dislocations for both approximations are presented in Fig. 12. The distribution of the order parameter η and shear stress σ_{xy} at $x = 19$ at $t = 20$ are also presented for the lower degree approximation (dashed red line), and for the higher degree approximation (blue solid line) in Fig. 13. While for the higher degree approximation (Fig. 12b), there are 2 and 3 dislocations in the second and third systems (from the bottom), respectively, for the lower degree approximation (Fig. 12a), the second dislocation in the second system did not completely pass through the band and 3 dislocations appeared in the third system.

Note that for both approximations the height of the second dislocation in the upper band is smaller than the prescribed value H^α. The reason is that the plastic shear less than $2\gamma_\alpha$ (and Burgers vector less than $2|\boldsymbol{b}^\alpha|$) is required to relax stresses. One of the possible solutions would be like in a third band in Fig. 12b, when the second dislocation is arrested within a sample. However, for the upper band, the second complete dislocation is too close to the free surface and it is energetically more favorable that it reaches the surface and exits the sample but it is incomplete in the entire band (i.e., produces plastic shear less than $2\gamma_\alpha$). Thus, it represents a *surface-modified partial dislocation*. To some extent, it is similar to surface-induced martensitic pre-transformations

[69] or premelting (partial disordering) [68]. Namely, while in bulk thermodynamically equilibrium Burgers vector or transformation strain is fixed, the surface can equilibrate some non-complete Burgers vector or transformation strain.

Next step for this problem is the propagation of an austenite-martensite interface with the inheritance or pushing of the generated dislocation. Such a problem within the sharp interface approach and the phenomenological isotropic plasticity has been solved in [64], with the prescribed interface advance. The phase field approach will provide a much more precise and flexible tool for the solution of this problem, including the arrest of the martensitic unit. Such an arrest determines a plate/lath morphological transition and is of fundamental and applied importance for material design and achieving desired mechanical properties.

4.4. Dislocation activity in a nanograin bicrystal under plastic shear and pressure

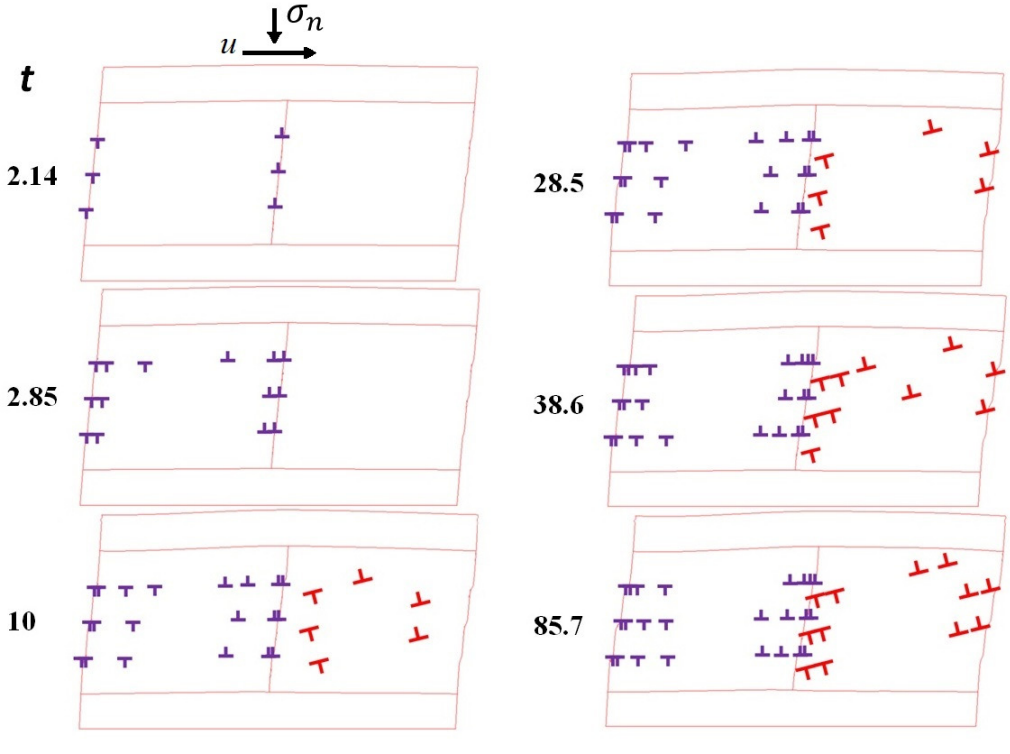

Fig. 14: Schematics of a sample with two nanograins under compression and shear with a stationary dislocation nanostructure at the prescribed $\gamma_b = 0.2$ with stationary values of $p = 4.3$ and $\tau = 2.6$ in the left grain, and $p = 5.3$ and $\tau = 5.5$ in the right grain Evolution of dislocations in both grains are presented as well.

Simple shear represents the main mechanism of plastic flow and it is of great importance

for the synthesis of nanograin materials and producing strain-induced phase transformations, in particular under high pressure. Such a loading can be produced under torsion or high-pressure torsion [4, 44]. Superposition of high pressure and large plastic shear in rotational Bridgman anvils [39] and rotational diamond anvil cell [7, 54, 56, 76] leads to unique results, namely, to new phases or known phases under much lower pressure than under hydrostatic conditions. This topic is under intense study at the nanoscale [56, 57, 72, 74]. The following mechanism for a significant reduction of the transformation pressure due to the plastic shear was suggested: shear stresses produce dislocation pile-ups with strong stress concentrations, which lead to barrierless martensite nucleation. However, if in experiment the pressure is lower than the critical value required for the phase transformation, the stress concentration can relax due to additional plasticity (rather than the phase transformation), and the produced dislocation structure may suppress the transformation rather than to promote [56, 57]. Here, we solve a problem on dislocation evolution under a prescribed simple shear in a nanosize bicrystal to understand how slip transfers from one grain to another and the resulting dislocation structure. In the future work, these results will be used as initial conditions for studying phase transformations under pressure and shear. Nanograins are chosen because large plastic deformations lead to nanograin structures.

A rectangular sample is considered with the size of 142.8×85.7, which includes the following regions (Fig. 14): (a) two grains of the size of 71.4×57.1 each, in which dislocations are studied; (b) two regions of the size of 142.8×14.3 located at the top and bottom of the sample, where only the mechanical problem is solved; these regions model elastic accommodation of the grains that surround two grains with plasticity. For the mechanical problem, periodic conditions for displacements are prescribed for lateral sides; the bottom horizontal side is fixed; the upper side is subjected to normal homogenous stress σ_n in the deformed state and homogeneous horizontal displacement u.

A vertical stress $\sigma_n = 8.8$ is considered, which results in an initial pressure averaged over the sample (or each grain) of 5.77. The average pressure is defined as $p = -0.5(\sigma_x + \sigma_y)$. Also, the following homogeneous horizontal displacement is applied at the upper side: $u = 8.57$ from $t = 0$ to 28.6, then $u = 0.2t$ from $t = 28.6$ to 42.8, and finally $u = 11.4$ from $t = 42.8$ to 85.7. The horizontal displacement is given in terms of prescribed macroscopic shear $\gamma_b = u/h$, with the height of grains $h = 57.1$.

We consider three horizontal slip systems in the left grain (defined by the order parameter η_1), and three slip systems inclined under 15^0 in the right grain (defined by order parameter η_2) (Fig. 14). This example, in particular, shows the capability of our PF model to obtain a mesh-independent solution for dislocations for any orientation. Initial conditions are $\eta_1 = 0.01$ and

$\eta_2 = 0.01$ inside the dislocation band in the left and right grains, respectively. Under the prescribed pressure and shear, first, dislocations of the opposite sign appear at the grain boundaries of the left grain and move toward each other. After 3 dislocation pairs appeared in the left grain, the first dislocation pairs appeared in the right grain In the following, by increasing shear, more dislocations are generated in both grains, with 5 and 2 dislocations in the right and left grains for the stationary state, respectively. The evolution of dislocation systems for both grains is presented in Fig. 14. As can be seen, after the nucleation and propagation, some of dislocations leave the dislocation bands, creating steps at the end of the band, and some others create dislocation pile-ups near the grain boundary. In the left grain, 2 dislocations of the positive sign and 2 dislocations of the negative sign leave the upper band from the right and left sides, respectively, and 3 dislocations of the positive sign and 3 dislocations of the negative sign create pile-ups at the right and left sides, respectively. For the middle and lower bands, only one dislocation leaves the band from each side of the band, and 3 dislocations of the positive sign and 3 dislocations of the negative sign create pile-ups at the right and left sides, respectively.

In the right grain, for the upper band, 1 dislocation of the negative sign leaves the left grain, and another negative dislocation is arrested near it, while 2 positive dislocations are stuck inside the grain For the middle band, 1 positive and 1 negative dislocations leave the upper band from the right and left sides, respectively, and 1 positive and 1 negative dislocations are equilibrated near them. For the lower band, 1 positive dislocation leaves the band from the right end and 1 positive and 2 negative dislocations create pile-ups at the right and left ends, respectively. Average pressure and shear stress are relaxed during dislocation generation. As shown in Fig. 15, the pressure monotonically reduces during dislocation generation even when the applied shear is increased from $u = 8.6$ to $u = 11.4$. The pressure is reduced from the initial value of $p = 5.5$ to the stationary values of $p = 4.1$ and $p = 5.1$ for the left and right grains, respectively. After applying $u = 8.6$, the average shear stress reduces due to the dislocation generation from the initial value of $\tau = 7.4$ to $\tau = 2$ and $\tau = 4.5$ for the left and right grains, respectively. Then, it is increased in both grains due to the larger applied shear $u = 8.6 + 0.2t$ from $t = 28.6$ to 42.8. However, due to the generation of dislocations, it reduces in the left grain even when the applied shear is still increasing to $u = 11.4$. Finally, after applying constant shear $u = 11.4$, the average shear stress reduces to the stationary values of $\tau = 2.6$ and 5.5 for the left and right grains respectively. The larger reduction of the average pressure and shear stress in the left grain is due to the generation of the larger number of dislocations compared to that in the right grain

Note that we used two different order parameters η_1 and η_2 in order to avoid direct passing dislocations through grain boundary. Alternatively, one can use just one order parameter and

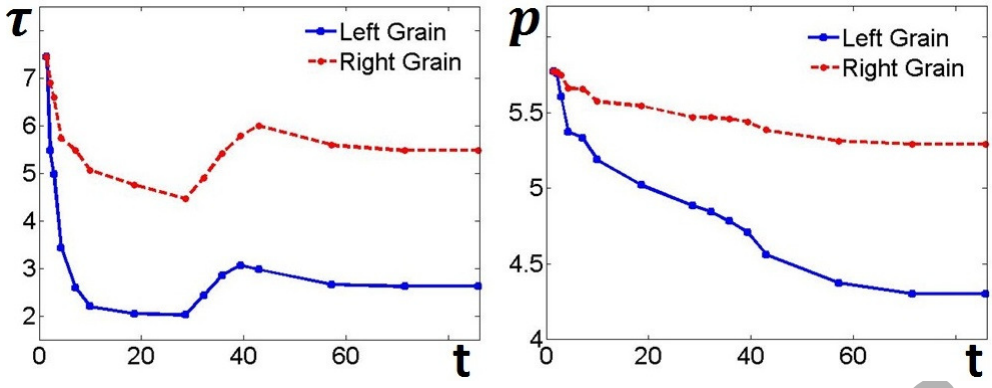

Fig. 15: Pressure and shear stress vs. time during dislocation activity until it reaches the stationary state at $t = 85.7$.

+

rotate the slip system across the boundary. To avoid the direct passing dislocations through the grain boundary in this case, one needs to introduce a finite-width boundary with $\eta = 0$.

4.5. Interaction of two dislocation systems

The objectives of this section are:

(1) To study the effect of the new term in the thermodynamic potential that describes the interaction of the cores of different dislocations when they pass through the same region.

(2) To demonstrate a mesh-independent solution for arbitrary inclined slip systems.

(3) To make the first step in studying phase transformations at a shear-band intersection, which is the main mechanism of strain-induced phase transformations in TRIP steels [16, 15]. This problem was studied within the simplified macroscopic theory in [63].

Since the actual value of the magnitude of the interaction term, A_{12}, is unknown, three cases will be considered:

(a) Without the interaction term, $A_{12} = 0$.

(b) With the interaction term $I_1 = A_{12}\bar{\eta}_1^2(1-\bar{\eta}_1)^2\bar{\eta}_2^2(1-\bar{\eta}_2)^2$ that penalizes the interaction of η_1 and η_2 dislocations at the same point with a small $A_{12} = 0.1A$. We will see that such a small interaction affects the local dislocation structure but does not affect the averaged stress-time curve.

(c) A simpler interaction term, $I_2 = A_{12}\bar{\eta_1}^2\bar{\eta_2}^2$, which, however, does not satisfy condition (21), with $A_{12} = 0.1A$. Nevertheless, the main difference between the two interaction terms is in the magnitude of their contributions. For example, for $\bar{\eta_1} = \bar{\eta_2} = 0.5$, one has $I_2 = \bar{\eta_1}^2\bar{\eta_2}^2 = 1/16$ and $I_1 = \bar{\eta}_1^2(1-\bar{\eta}_1)^2\bar{\eta}_2^2(1-\bar{\eta}_2)^2 = 1/256$, i.e., they differ by a factor of 16. In this case, both

the local structure and the global stress-time curve are significantly different. It is clear that for a similar or larger magnitude of the interaction term I_1, the both local and global effects will be significant as well.

Two dislocation systems with the angle 60^0 between them are located inside a rectangle with the size of 22.8×68.6 (Fig. 16). The lower side is fixed in the x and y directions, the upper side is fixed in the x direction and the vertical displacement $v = -(2.8 + 0.2t)$ is applied from $t = 0$ to 30. Lateral sides are free. Initial conditions for dislocations are $\eta_1 = -0.01$ in a small region at the right end of the dislocation system with $+60^0$ inclination with respect to the x direction (shown with blue dislocation signs) and $\eta_2 = -0.01$ in a small region at the left end of the other system (shown with pink dislocation signs). The plastic shear $\gamma_\alpha = 0.25$ and $w = H$. Note that the dislocations interact through their stress field in any case. The evolution of dislocation systems without the interaction term is plotted in Fig. 16. Solution is symmetric with respect to both dislocation systems. First dislocations appear in each slip system in the lower part of the sample and propagate to the intersection region at the center of the sample ($t = 1.6$). While the lowest dislocations pass through ($t = 2.1$), two other dislocations stuck for some time, which leads to nucleation of the second dislocations in both systems in the upper part of the sample. However, when the first dislocations pass through the center ($t = 10.1$), the second dislocations disappear. The same process repeats itself for the second ($t = 15.6$) and third dislocations ($t = 24.3$). Dislocations pass through the entire sample and make steps at both free surfaces.

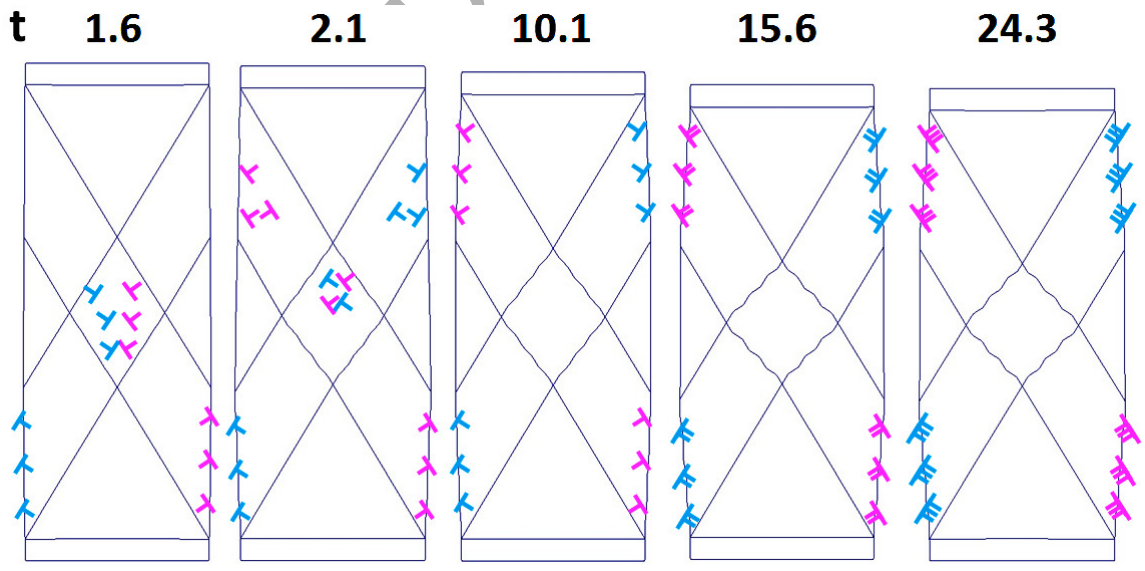

Fig. 16: Evolution of dislocation systems under prescribed compressive displacement without the penalty term for interaction between dislocations.

The evolution of dislocations when the interaction term $I_1 = A_{12}\bar{\eta}_1^2(1-\bar{\eta}_1)^2\bar{\eta}_2^2(1-\bar{\eta}_2)^2$ is included is presented in Fig. 17. First dislocations of both η_1 and η_2 systems appear at free

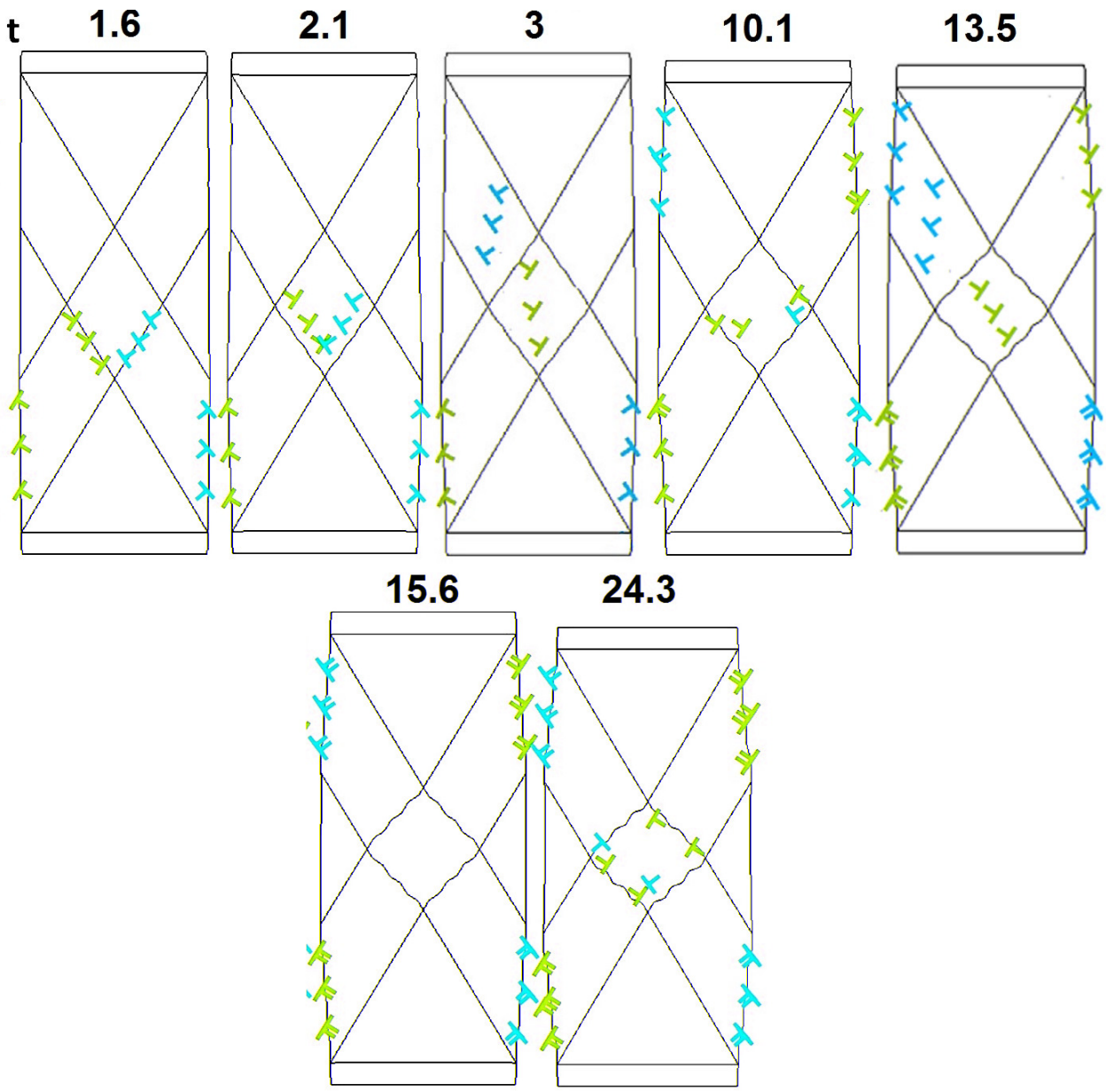

Fig. 17: Evolution of dislocation systems under prescribed compressive displacement with consideration of the penalty term $I_1 = A_{12}\bar{\eta}_1^2(1-\bar{\eta}_1)^2\bar{\eta}_2^2(1-\bar{\eta}_2)^2$ for interaction between dislocations.

surfaces and then are temporarily arrested at the intersection zone ($t = 1.6$ and $t = 2.1$). After this time instant, system loses its symmetry with respect to two dislocation systems. After η_2 dislocations move completely away from the intersection zone ($t = 3$), η_1 dislocations pass through it. Second dislocations of η_2 system in the upper and middle bands appear at the free surface. While the second dislocations in the middle band pass through the sample ($t = 10.1$), dislocations in the upper band first are temporarily arrested at the intersection but then pass through the sample ($t = 13.5$). At the same time, second dislocations of η_1 system appear at the free surface but are for a while arrested at the intersection zone. After the η_2 dislocations pass through the

intersection ($t = 13.5$), the η_1 dislocations can pass through as well. At $t = 1.6$ two dislocations reach free surface in each slip system, and results are symmetric with respect to exchange of η_1 and η_2. Third dislocations of both η_1 and η_2 systems appear at the free surfaces of both sides, move toward the interaction zone, and then dislocations of η_2 system pass through the interaction zone ($t = 24.3$) while the dislocations of η_1 system stay at the intersection zone. After the η_2 dislocations pass through the intersection, the η_1 dislocations can pass through as well. The shear strain ε_{xy} is plotted in the deformed state for $t = 24.3$ in Fig. 19. It is localized inside the dislocation bands of both systems and does not spread between dislocation bands.

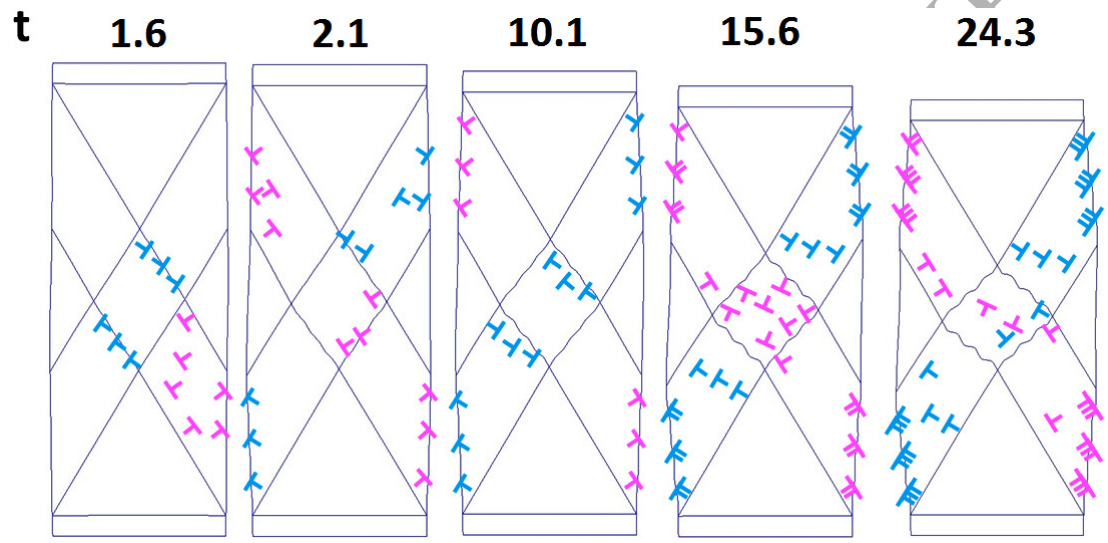

Fig. 18: Evolution of dislocation systems under prescribed compressive displacement with consideration of the penalty term $I_2 = A_{12}\bar{\eta_1}^2\bar{\eta_2}^2$ for interaction between dislocations.

A simpler interaction term, $I_2 = A_{12}\bar{\eta_1}^2\bar{\eta_2}^2$, which, however, does not satisfy condition II, has been studied as well (Fig. 18). Stronger interaction between two systems leads to highly nonsymmetric solution from the very beginning, see $t = 1.6$ and $t = 2.1$. Due to the penalty term some dislocations are generated only at one side of the intersection zone and do not pass through the sample, and consequently make a step only at one free surface ($t = 1.6$ to 15.6). Other dislocations, which pass through the entire sample, make steps at both free surfaces. Note that both penalty terms do not completely eliminate simultaneous presence of dislocations belonging to different systems in the same region (see $t = 24.3$).

To show the effect of the penalty term on the averaged stress, the average vertical normal stress vs. time is plotted for the problems with two different types of the interaction term and without it in Fig. 20. Due to the constant displacement $v = 2.8$ at $t = 0$, the initial stress is high, which is relaxed due to the generation of first dislocations for both problems. In the following, the stress is increased by applying the growing displacement $v = 2.8 + 0.2t$. While there is an essential

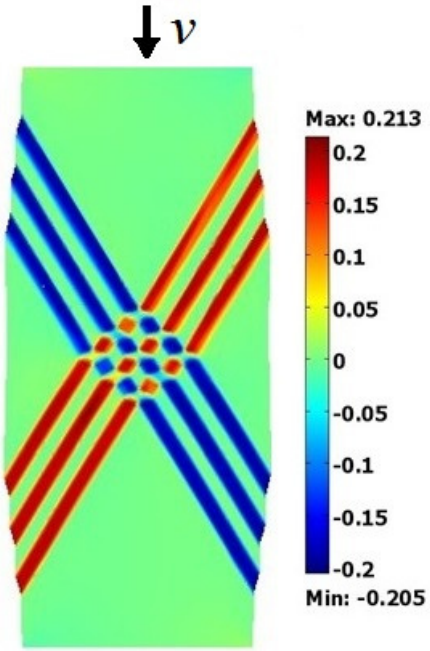

Fig. 19: The shear strain ε_{xy} at $t = 24.3$ for the problem with the interaction term $I_1 = A_{12}\bar{\eta}_1^2(1-\bar{\eta}_1)^2\bar{\eta}_2^2(1-\bar{\eta}_2)^2$.

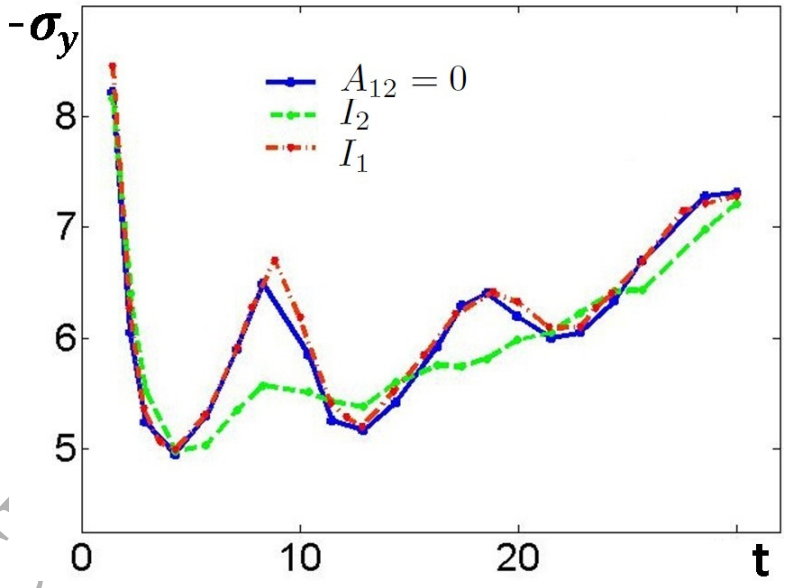

Fig. 20: Average vertical compressive stress $(-\sigma_y)$ vs. time during dislocation evolution until $t = 30$ without penalizing term ($A_{12} = 0$), with the simplified penalizing term $I_2 = A_{12}\bar{\eta_1}^2\bar{\eta_2}^2$, and with penalizing term $I_1 = A_{12}\bar{\eta}_1^2(1-\bar{\eta}_1)^2\bar{\eta}_2^2(1-\bar{\eta}_2)^2$.

difference in the dislocation structure, the curves for stresses without and with the interaction term I_1 are very close. This is because of a relatively small magnitude of the interaction term. With increasing A_{12}, the deviation of the two curves increases. For the problem without the interaction term, the stress drops two more times due to the generation of second and third dislocations. However, it generally increases due to the growing applied displacement. For the problem with the interaction term $I_2 = A_{12}\bar{\eta}_1^2\bar{\eta}_2^2$, after the first dislocations appear, the stress smoothly increases

without significant oscillation. The reason is that dislocations can be generated not only from the free surfaces, but also due to the stress concentration at temporarily arrested dislocations. This promotes dislocation generation, and consequently stress relaxation. That is why the stress does not significantly increase under growing applied displacement and varies quite smoothly. Note that the stress is generally lower than for the problem without the interaction due to the larger number of dislocations. At the same time, such an additional dislocation nucleation does not happen for the interaction term due to the the lack of stress concentration.

The curve for the averaged stress vs. time for the simplified interaction term significantly deviates from the two other cases, mostly because of at least an order of magnitude larger interaction term. Few more dislocations are generated for this case than for the two other cases, which leads to lower stresses and a lack of intermediate stress peaks. Stress grows more smoothly with increasing strains.

5. Concluding remarks

The following points distinguish the current paper from the previous ones.

Our model: (a) includes large strain kinematics; (b) reproduces the desired, mesh-independent height of dislocation bands for any slip system orientation and prevents dislocation widening by introducing piece-wise periodic magnitude of the barrier coefficient; (c) excludes the localization of dislocation within a band of a smaller height than the prescribed one with the help of the gradient energy term along the normal to slip plane, which, however, does not produce artificial interface energy; (d) penalizes the interaction of different dislocations at the same point; (e) allows us to generate desired lattice instability conditions and a stress - order parameter curve, as well as to obtain stress-independent equilibrium Burgers vector and to avoid artificial dissipation during elastic deformation; (f) treats non-periodic boundary conditions for dislocations. While we focused here at the edge dislocations, a similar approach can be applied for screw dislocations; one just has to consider the Burgers vector parallel to the dislocation line.

Since none of the published numerical approaches based on the spectral methods were able to treat large strain problems and non-periodic boundary conditions, FEM is utilized here. Computational mechanical aspects of the phase field simulations of dislocation nucleation and evolution are addressed for the first time. The main focus was on proving that the new points of the developed theory can be confirmed in simulations, including possibility of obtaining the desired dislocation height for aligned and inclined dislocations, eliminating spurious stresses, resolving dislocation

cores and interaction between cores of different dislocations. The single dislocation order parameter profile and the stationary distance between two neighboring dislocations at a semicoherent austenite - martensite interface (problem that involves large strains) are in perfect agreement with analytical expressions. Mesh independence of the solutions is proved. The best approximating finite element polynomials are found that eliminate spurious stress oscillations at the boundaries between dislocation band and the rest of the crystal or between dislocation bands. The possibility of significant numerical errors is demonstrated for coarser mesh, non-regularized models, and not optimal approximating FEM polynomials. Analytical solutions for a stationary and propagating single dislocation, dislocation velocity, core energy, and core width are found. A calibration procedure is developed and dislocation parameters for nickel are identified based on existing molecular dynamics simulations. Problems of nucleation and evolution of multiple dislocations along the sharp austenite - martensite interface and along the single and multiple slip systems near martensitic lath, the activity of dislocations with two different orientations in a nanograined material under shear and pressure, and the interaction between two intersecting dislocation systems were studied. Surface-modified partial dislocation was revealed. Importance of the term describing interaction of cores of dislocations belonging to the different slip systems is demonstrated at the local and global level, depending on the magnitude of this term. These problems represent the first step in the future study of interaction of phase transformation and dislocations, in particular, for studying thermodynamics, kinetics, and mechanisms of propagation of semicoherent interfaces, arrest of lath martensite and plate-lath morphological transition, nucleation of strain-induced martensite at shear band intersection, and the effect of large plastic shear on high pressure phase transformations. The next step will be based on the generalization of the developed theory for the interaction between dislocations and phase transformations. Some of the first results in this direction are already obtained [71, 72, 73, 74].

We would like to note that our approach and previous phase field approaches and discrete dislocations approaches (e.g., [9, 12, 25, 29, 78]) do not compete because they are intended for different classes of problems and phenomena. We resolve dislocation core, use large strain formulation and non-periodic boundary conditions. Previous phase field approaches could not solve large strain problems and apply non-periodic boundary conditions. Discrete dislocations approaches are based on the theory of dislocations in linear elastic material and utilize principle of superposition, they do not resolve dislocation core and not applicable to large strain problems. However, due to simpler models and possibility of application of spectral methods and/or principle of superposition, these methods are numerically more efficient and allow treatment of a larger sample. Thus, they are more suitable for studying *global material behavior* while our approach is more effective when

short range interaction of dislocations and dislocations and other defects is of importance, like point defects, grain and twin boundaries, and phase interfaces.

At the same time, previous and current phase field approaches can benefit from each other. Since for periodic boundary conditions spectral methods proved to be effective, and there are currently promising developments of spectral approaches for large-strain macroscopic plasticity [36], it would be reasonable to try to combine these spectral methods and our large strain phase field approach. Also, considering of large dislocation height (i.e., a slip band instead of a single dislocation) can be and effective method for coarse-graining and scaling up our simulations. On the other hand, our thermodynamic potential and expression for plastic strain versus order parameters, which satisfy additional conditions, and provide desired stress-order parameter curve and stress-independent Burgers vector, can be utilized in existing small strain approaches. Similar, our methods to introduce the desired width of the dislocation through the theory can be implemented in the existing theories as well. Previous approaches can also benefit from the strict computational mechanics studies of the accuracy and grid dependence of the solutions, similar to those in the current paper. In particular, it would be of interest to determine what the level of inaccuracy is introduced by assuming that the dislocation height is equal to one intergrid space, in which cases it is acceptable, and how to improve accuracy without essential increase of computational cost.

Problems considered here could be solved using molecular dynamics method [41, 43]. As usual, any continuum and atomistic approaches do not compete but supplement each other. Continuum approach does not need to resolve atomic oscillation and can use much larger time step. Atomistic approach does not need special developments to treat large strains and to combine several phenomena, like dislocations and phase transformations. Due to completely different ways of introducing desired information and calibrating models, it is not completely clear which approach is more accurate for the given problem. For example, phase field approach describes melting temperature of nanoparticles of radii less than 5 nm essentially better than molecular dynamics [68].

Acknowledgments

The supports of NSF (DMR-1434613 and CMMI-1536925), ARO (W911NF-12-1-0340), DARPA (W31P4Q-13-1-0010), ONR, and Iowa State University (Schafer 2050 Challenge Professorship) are gratefully acknowledged.

References

[1] A. Dietsche, P. Steinmann, K. William, Micropolar elastoplasticity and its role in localization, Int. J. Plast. 9 (1993), 813-831.

[2] A. Hunter, C. Le, F. Saied, M. Koslowski, Large-scale 3D phase field dislocation dynamics simulations on high-performance architectures, Int. J. High Perform. Comput. Appl. 25 (2010), 223-235.

[3] A. Hunter, I. J. Beyerlein, T. C. Germann, M. Koslowski, Influence of the stacking fault energy surface on partial dislocations in fcc metals with a three-dimensional phase field dislocations dynamics model, Phys. Rev. B. 84 (2011), 144108.

[4] A. P. Zhilyaev, T. G. Langdon, Microstructure and microtexture evolution in pure metals after ultra-high straining, J. Mater. Sci. 47 (2000), 7888-7893.

[5] A. V. Idesman, V. I. Levitas, E. Stein, Structural changes in elastoplastic materials: a unified finite element approach for phase transformation, twinning and fracture, Int. J. Plast. 16 (2000), 893-949.

[6] A. V. Yanilkin, V. S. Krasnikov, A. Y. Kuksin, A. E. Mayer, Dynamics and kinetics of dislocations in Al and AlCu alloy under dynamic loading, Int. J. Plast. 55 (2014), 94-107.

[7] C. Ji, V. I. Levitas, H. Zhu, J. Chaudhuri, A. Marathe, Y. Ma, Shear-induced phase transition of nanocrystalline hexagonal boron nitride to wurtzitic structure at room temperature and lower pressure, Proc. Natl. Acad. Sci. U S A 109 (47) (2012), 19108-19112.

[8] C. Shen, Y. Wang, Incorporation of γ-surface to phase field model of dislocations: simulating dislocation dissociation in fcc crystals, Acta Mater. 52 (2004), 683-691.

[9] C. Zhou, S. B. Biner, R. LeSar, Discrete dislocation dynamics simulations of plasticity at small scales, Acta Mater. 58 (2010), 1565-1577.

[10] D. A. Porter, K. E. Easterling, Phase transformations in metals and alloys, Chapman & Hall, London, England, 1992.

[11] D. K. Satapathy, V. M. Kaganer, B. Jenichen, W. Braun, L. Dweritz, K. H. Plo, Periodic array of misfit dislocations at the MnAs/GaAs interface studied by synchrotron x-ray diffraction, Phys. Rev. B. 72 (2005), 155303.

[12] D. Li, H. Zbib, X. Sun, M. Khaleel, Predicting plastic flow and irradiation hardening of iron single crystal with mechanism-based continuum dislocation dynamics, Int. J. Plast. 52 (2014), 3-17.

[13] D. Rodney, Y. Le Bouar, A. Finel, Phase field methods and dislocations, Acta Mater. 51 (2003), 17-30.

[14] D.-W. Lee, H. Kim, A. Strachan, M. Koslowski, Effect of core energy on mobility in a continuum dislocation model, Phys. Rev. B. 83 (2011), 104101.

[15] G. B. Olson, Transformation plasticity and the stability of plastic flow. In: Deformation, Processing and Structure. ed G. Krauss, 391-424, ASM International, Warrendale, PA, 1984.

[16] G. B. Olson, M. Cohen, 1972. A mechanism for the strain-induced nucleation of martensitic transformation, J. Less-Common Metals. 28 (1972), 107.

[17] G. Cicero, Ab initio study of misfit dislocations at the SiC-Si(001) interface, Phys. Rev. Lett. 89 (2002), 156101.

[18] H. J. Chu, J. Wang, I. J. Beyerlein, E. Pan, Dislocation models of interfacial shearing induced by an approaching lattice glide dislocation, Int. J. Plast. 41 (2013), 1-13.

[19] H. M. Zbib, C. T. Overman, F. Akasheh, D. Bahr, Analysis of plastic deformation in nanoscale metallic multilayers with coherent and incoherent interfaces, Int. J. Plast. 27 (2011), 1618-1639.

[20] J. Chaussidon, C. Robertson, D. Rodney, M. Fivel, Dislocation dynamics simulations of plasticity in Fe laths at low temperature, Acta Mater. 56 (2008), 5466-5476.

[21] J. Fan, R. J. Stewart, X. Zeng, A multiscale method for dislocation nucleation and seamlessly passing scale boundaries, Int. J. Plast. 27 (2011), 2103-2124.

[22] J. Kundin, H. Emmerich, J. Zimmer, Mathematical concepts for the micromechanical modelling of dislocation dynamics with a phase-field approach, Philos. Mag. 91 (2011), 97-121.

[23] J. Pamin, R. De Borst, A gradient plasticity approach to finite element predictions of soil instability, Arch. Mech. 47 (1995), 353-377.

[24] J. R. Mayeur, D. L. McDowell, A three-dimensional crystal plasticity model for duplex Ti-6Al-4V, Int. J. of Plast. 23 (2007), 1457-1485.

[25] J. Senger, D. Weygand, P. Gumbsch, O. Kraft, Discrete dislocation simulations of the plasticity of micro-pillars under uniaxial loading, Scripta Mater. 58 (2005), 587-590.

[26] K. Kang, J. Wang, S. J. Zheng, J. J. Beyerlein, Minimum energy structures of faceted, incoherent interfaces, Appl. Phys. Lett. 112 (2012), 073501.

[27] L. Lei, M. Koslowski, Mesoscale modeling of dislocations in molecular crystals, Philos. Mag. 91 (2011), 865-878.

[28] L. Xiong, D. L. McDowell, Y. Chen, Sub-THz Phonon drag on dislocations by coarse-grained atomistic simulations, Int. J. Plast. 55 (2014), 268-278.

[29] M. Huang, L. Zhao, J. Tong, Discrete dislocation dynamics modelling of mechanical deformation of nickel-based single crystal superalloys, Int. J. Plast. 28 (2012), 141-158.

[30] M. Koslowski, Scaling laws in plastic deformation, Phil. Mag. 87 (2007), 1175-1184.

[31] M. Koslowski, A. M. Ortiz, A multi-phase field model of planar dislocation networks, Model. Simul. Mater. Sci. Eng. 12 (2004), 1087-1097.

[32] M. Koslowski, M. Cuitino, A. M. Ortiz, A phase-field theory of dislocation dynamics, strain hardening and hysteresis in ductile single crystals, J. Mech. Phys. Solids. 50 (2002), 2597-2635.

[33] M. S. Öztop, C. F. Niordson, J. W. Kysar, Length-scale effect due to periodic variation of geometrically necessary dislocation densities, Int. J. Plast. 41 (2013), 189-201.

[34] N. Abdolrahim, H. M. Zbib, D. F. Bahr, Multiscale modeling and simulation of deformation in nanoscale metallic multilayer systems, Int. J. Plast. 52 (2014), 33-50.

[35] P. Cermelli, M. E. Gurtin, On the kinematics of incoherent phase transitions, Acta. Mater. 42 (1994), 3349-3359.

[36] P. Eisenlohr, M. Diehl, R. A. Lebensohn, F. Roters, A spectral method solution to crystal elasto-viscoplasticity at finite strains, Int. J. Plast. 46 (2013), 37-53.

[37] P. Engels, A. Ma, A. Hartmaier, Continuum simulation of the evolution of dislocation densities during nanoindentation, Int. J. Plast. 38 (2012), 159-169.

[38] P. Perzyna, Instability phenomena and adiabatic shear-band localization in thermoplastic flow processes, Acta Mater. 106 (1994), 173-205.

[39] P. W. Bridgman, Effect of high shear stress combined with high hydrostatic pressure, Phys. Rev. 48 (1995), 825-847.

[40] R. F. Zhang, J. Wang, I. J. Beyerlein, A. Misra, Interface dislocation patterns and dislocation nucleation in face-centered-cubic and body-centered-cubic bicrystal interfaces, Int. J. Plast. 53 (2014), 40-55.

[41] R. F. Zhang, J. Wang, I. J. Beyerlein, A. Misra, T. C. Germann, Atomic-scale study of nucleation of dislocations from fcc-bcc interfaces, Acta Mater. 60 (2012), 2855-2865.

[42] R. F. Zhang, J. Wang, I. J. Beyerlein, T. C. Germann, Dislocation nucleation mechanisms from fcc/bcc incoherent interfaces, Scripta Mater. 65 (2011), 1022-1025.

[43] R. Ravelo, T. C. Germann, O. Guerrero, Q. An, B. L. Holian, Shock-induced plasticity in tantalum single crystals: interatomic potentials and large-scale molecular-dynamics simulations, Phys. Rev. B. 88 (2013), 134101.

[44] R. Z. Valiev, R. K. Islamgaliev, I. V. Alexandrov, Bulk nanostructured materials from severe plastic deformation, Prog. Mat. Sci. 45 (2000), 103-189.

[45] S. Maheswaran, S. Thevuthasan, F. Gao, V. Shutthanandan, C. M. Wang, R. J. Smith, Misfit dislocations at the single-crystal Fe_2O_3/Al_2O_3 interface, Phys. Rev. B. 72 (2005), 075403.

[46] S. S. Quek, Y. Xiang, D. J. Srolovitz, Loss of interface coherency around a misfitting spherical inclusion, Acta Mater. 59 (2011), 5398-5410.

[47] S. Y. Hu, L. Q. Chen, Solute segregation and coherent nucleation and growth near a dislocation - a phase-field model integrating defect and phase microstructures, Acta. Mater. 49 (2001), 463-472.

[48] S. Y. Hu, L. Q. Chen, Diffuse-interface modeling of composition evolution in the presence of structural defects, Comput. Mater. Sci. 23 (2002), 270-282.

[49] S. Y. Hu, Y. L. Li, Y. X. Zheng, L. Q. Chen, Effect of solutes on dislocation motion - a phase-field simulation, Int. J. Plast. 20 (2004), 403-425.

[50] T. M. Hatem, M. A. Zikry, Dislocation-density crystalline plasticity modelling of lath martensitic microstructures in steel alloys, Philos. Mag. 89 (2009), 3087-3109.

[51] T. M. Hatem, M. A. Zikry, Dynamic shear-strain localization and inclusion effects in lath martensitic steels subjected to high pressure loads, J. Mech. Phys. Solids. 58 (2010), 1057-1072.

[52] T. Zhu, C. Y. Wang, Misfit dislocation networks in the γ/γ' phase interface of a Ni-based single-crystal superalloy: Molecular dynamics simulations. Phys. Rev. B. 72 (2005), 014111.

[53] V. A. Vorontsov, C. Shen, Y. Wang, D. Dye, C. M. F. Rae, Shearing of γ' precipitates by $a < 112 >$ dislocation ribbons in Ni-base superalloys: a phase field approach, Acta Mater. 58 (2004), 4110-4119.

[54] V. D. Blank, M. Popov, S. G. Buga, V. Davydov, V. N. Denisov, A. N. Ivlev, B. N. Mavrin, V. Agafonov, R. Ceolin, H. Szwarc, A. Passat, Is C_{60} fullerite harder than diamond?, Phys. Lett. A. 188 (1994), 281-286.

[55] V. I. Levitas, Structural changes without stable intermediate state in inelastic material. Part II. Applications to displacive and diffusional-displacive phase transformations, strain-induced chemical reactions and ductile fracture, Int. J. Plast. 16 (2000), 851-892.

[56] V. I. Levitas, Continuum mechanical fundamentals of mechanochemistry. In: High Pressure Surface Science and Engineering. Section 3. Ed. Y. Gogotsi and V. Domnich, Institute of Physics Publishing, 159-292, 2004.

[57] V. I. Levitas, High-pressure mechanochemistry: conceptual multiscale theory and interpretation of experiments, Phys. Rev. B. 70 (2004), 184118.

[58] V. I. Levitas, Interface stress for nonequilibrium microstructures in the phase field approach: exact analytical results, Phys. Rev. B. 87 (2013), 054112.

[59] V. I. Levitas, Phase-field theory for martensitic phase transformations at large strains. Int. J. Plast. 49 (2013), 85-118.

[60] V. I. Levitas, Thermodynamically consistent phase field approach to phase transformations with interface stresses, Acta Mater. 61 (2013), 4305-4319.

[61] V. I. Levitas, A. V. Idesman, D.-W. Lee, Interface propagation and microstructure evolution in phase field models of stress-induced martensitic phase transformations, Int. J. Plast. 25 (2010), 395-422.

[62] V. I. Levitas, A. V. Idesman, E. Stein, Finite element simulation of martensitic phase transitions in elastoplastic materials, Int. J. Solids. Struct. 35 (1998), 855-887.

[63] V. I. Levitas, A. V. Idesman, G. B. Olson, Continuum modeling of strain-induced martensitic transformation at shear-band intersections, Acta Mater. 47 (1998), 219-233.

[64] V. I. Levitas, A. V. Idesman, G. B. Olson, E. Stein, Numerical modeling of martensite growth in elastoplastic material, Philos. Mag. A. 82 (2002), 429-462.

[65] V. I. Levitas, D. L. Preston, Three-dimensional Landau theory for multivariant stress-induced martensitic phase transformations. I. Austenite–martensite, Phys. Rev. B. 66 (2002), 134206.

[66] V. I. Levitas, D. L. Preston, Three-dimensional Landau theory for multivariant stress-induced martensitic phase transformations. II. Multivariant phase transformations and stress space analysis, Phys. Rev. B. 66 (2002), 134207.

[67] V. I. Levitas, D. L. Preston, D.-W. Lee, Three-dimensional Landau theory for multivariant stress-induced martensitic phase transformations. III. Alternative potentials, critical nuclei, kink solutions, and dislocation theory, Phys. Rev. B. 68 (2003), 134201.

[68] V. I. Levitas, K. Samani, Size and mechanics effects in surface-induced melting of nanoparticles, Nat. Commun. 2 (2011), 284.

[69] V. I. Levitas, M. Javanbakht, Surface-induced phase transformations: multiple scale and mechanics effects and morphological transitions, Phys. Rev. Lett. 107 (2011), 175701.

[70] V. I. Levitas, M. Javanbakht, Advanced phase-field approach to dislocation evolution, Phys. Rev. B. Rapid Communications. 86 (2012), 140101.

[71] V. I. Levitas, M. Javanbakht, Phase field approach to interaction of phase transformation and dislocation evolution, Appl. Phys. Lett. 102 (2013), 251904.

[72] V. I. Levitas, M. Javanbakht, Phase transformations in nanograin materials under high pressure and plastic shear: nanoscale mechanisms, Nanoscale 6 (2014), 162-166.

[73] Levitas, V. I., Javanbakht. M. Interaction between phase transformations and dislocations at the nanoscale. Part 1. General phase field approach. J. Mech. Phys. Solids, 82 (2015) 287-319.

[74] Javanbakht, M. Levitas, V. I. Interaction between phase transformations and dislocations at the nanoscale. Part 2. Phase field simulation examples. J. Mech. Phys. Solids, 82 (2015) 164-185.

[75] V. I. Levitas, M. Javanbakht, Thermodynamically consistent phase field approach to dislocation evolution at small and large strains, J. Mech. Phys. Solids, 82 (2015), 345-366.

[76] V. I. Levitas, Y. Ma, E. Selvi, J. Wu, J. A. Patten, High-density amorphous phase of silicon carbide obtained under large plastic shear and high pressure, Phys. Rev. B. 85 (2012), 054114.

[77] V. Nagarajan, C. L. Ji, H. Kohlstedt, R. Waser, I. B. Misirlioglu, S. P. Alpay, R. Ramesh, Misfit dislocations in nanoscale ferroelectric heterostructures, Appl. Phys. Lett. 86 (2005), 192910.

[78] V. S. Deshpande, A. Needleman, E. van der Giessen, Plasticity size effects in tension and compression of single crystals, J. Mech. Phys. Solids. 53 (2005), 2661-2691.

[79] Y. M. Jin, A. G. Khachaturyan, Phase field microelasticity theory of dislocation dynamics in a polycrystal: model and three-dimensional simulations, Philos. Mag. 81 (2001), 607-616.

[80] Y. N. Cui, P. Lin, Z. L. Liu, Z. Zhuang, Theoretical and numerical investigations of single arm dislocation source controlled plastic flow in FCC micropillars, Int. J. Plast. 55 (2014), 279-292.

[81] Y. U. Wang, J. Li, Phase field modeling of defects and deformation, Acta. Mater. 58 (2010), 1212-1235.

[82] Y. U. Wang, Y. M. Jin, A. G. Khachaturyan, Phase field microelasticity modeling of dislocation dynamics near free surface and in heteroepitaxial thin films, Acta. Mater. 51 (2003), 4209-4223.

[83] Y. U. Wang, Y. M. Jin, A. M. Cuitino, A. G. Khachaturyan, Application of phase field microelasticity theory of phase transformations to dislocation dynamics: model and three-dimensional simulations in a single crystal, Philos. Mag. 81 (2001), 385-393.

[84] Y. U. Wang, Y. M. Jin, A. M. Cuitino, A. G. Khachaturyan, Nanoscale phase field microelasticity theory of dislocations: model and 3D simulations, Acta Mater. 49 (2001), 1847-1857.

[85] Y. U. Wang, Y. M. Jin, A. M. Cuitino, A. G. Khachaturyan, Phase field microelasticity theory and modeling of multiple dislocation dynamics, Appl. Phys. Lett. 78 (2001), 2324-2326.

[86] Z. L. Liu, Z. Zhuang, X. M. Liu, X. C. Zhao, Z. H. Zhang, A dislocation dynamics based on higher-order crystal plasticity model and applications on confined thin-film plasticity, Int. J. Plast. 27 (2011), 201-216.